Fermi National Accelerator Laboratory

FERMILAB-Pub-80/27-EXP
7120.069

(Submitted to Phys. Rev.)

THE REAL PART OF THE FORWARD ELASTIC NUCLEAR AMPLITUDE FOR pp, $\bar{p}p$, π^+p, π^-p, K^+p, AND K^-p SCATTERING BETWEEN 70 AND 200 GeV/c

L. A. Fajardo, R. Majka, J. N. Marx, P. Némethy, L. Rosselet,
J. Sandweiss, A. Schiz, and A. J. Slaughter
Yale University, New Haven, Connecticut 06520

and

C. Ankenbrandt, M. Atac, R. Brown, S. Ecklund, P. J. Gollon,
J. Lach, J. MacLachlan, A. Roberts, and G. Shen
Fermi National Accelerator Laboratory, Batavia, Illinois 60510

March 1980

Operated by Universities Research Association Inc. under contract with the United States Department of Energy

The Real Part of the Forward Elastic Nuclear Amplitude for pp, $\bar{p}p$, π^+p, π^-p, K^+p, and K^-p Scattering Between 70 and 200 GeV/c

L.A.Fajardo, R. Majka,[a] J. N. Marx,[a] P. Némethy,[a] L. Rosselet,[b]
J. Sandweiss, A. Schiz,[c] and A. J. Slaughter
Yale University
New Haven, Conneticut 06520

and

C. Ankenbrandt, M. Atac, R. Brown,[d] S. Ecklund,[e] P. J. Gollon,[f]
J. Lach, J. Maclachlan, A. Roberts, and G. Shen[g]
Fermi National Accelerator Laboratory
Batavia, Illinois 60510

ABSTRACT

We have measured the elastic cross section for pp, $\bar{p}p$, π^+p, π^-p, K^+p, and K^-p scattering at incident momenta of 70, 100, 125, 150, 175, and 200 GeV/c. The range of the four-momentum transfer squared, t, varied with the beam momentum from $0.0016 \leq -t \leq 0.36$ $(GeV/c)^2$ at 200 GeV/c to $0.0018 \leq -t \leq 0.0625$ $(GeV/c)^2$ at 70 GeV/c. The conventional parametrization of the t-dependence of the nuclear amplitude by a simple exponential in t was found to be inadequate. An excellent fit to the data was obtained by a parametrization motivated by the additive quark model. Using this parametrization we determined the ratio of the real to the imaginary part of the nuclear amplitude by the Coulomb interference method.

INTRODUCTION

Dispersion relations for nuclear scattering are based on the assumptions of unitarity, analyticity, and crossing symmetry and on the energy dependence of the total cross section. Measurements of the real part of the elastic nuclear amplitude provide a means of checking the validity of these assumptions and allow a glimpse at the behavior of the total cross sections at higher energies.

We have measured the elastic differential cross section for pp, $\bar{p}p$, π^+p, π^-p, K^+p, and K^-p scattering. The measurements were made at Fermilab with incident momenta of 70, 100, 125, 150, 175, and 200 GeV/c. The high spatial resolution of our apparatus allowed a very accurate determination of the scattering angle and thus of the four-momentum transfer squared, t. The t range of of the measurements depended on the incident momentum and varied from $0.0018 \leq -t \leq 0.0625\ (\mathrm{GeV}/c)^2$ at 70 GeV/c to $0.0016 \leq -t \leq 0.36\ (\mathrm{GeV}/c)^2$ at 200 GeV/c.

The real part of the forward nuclear amplitude has been measured extensively for pp scattering up to ISR energies.[1] The real parts for π^-p scattering have been measured[2] up to 140 GeV/c, while for π^+p and K^+p scattering are known[3,4] up to 52 GeV/c. The real parts for K^-p and $\bar{p}p$ scattering have not been measured[5,6] above 15 GeV/c. Our experiment measured three reactions simultaneously (pp, π^+p, K^+p and pp, π^-p, K^-p) and measured all six reactions with the same apparatus.

In the t range studied in this experiment the differential cross section is determined by both the Coulomb and nuclear scattering amplitudes:

$$d\sigma/dt = \pi \mid f_C + f_n \mid^2 \qquad (1)$$

At small -t the Coulomb amplitude is dominant and is given by the expression:

$$f_C = (2z_a e^2/c)\ G_a(t)\ G_p(t)\ \exp(iz_a \Omega)\ /\ t\ , \qquad (2)$$

where $z_a e$ is the charge of the incident particle a. $G_a(t)$ and $G_p(t)$ are the electromagnetic form factors of the incident particle a and the target proton. We use the dipole form for the protons and the monopole form for the pions and kaons:

$$G_p(t) = 1\ /\ (1 + v_p\ |t|)^2 \qquad (3a)$$

$$G_\pi(t) = 1\ /\ (1 + 2v_\pi\ |t|) \qquad (3b)$$

$$G_K(t) = 1\ /\ (1 + 2v_K\ |t|) \qquad (3c)$$

$$v_p = r_p{}^2\ /\ 12\hbar^2$$

$$v_\pi = r_\pi{}^2\ /\ 12\hbar^2$$

$$v_K = r_K{}^2\ /\ 12\hbar^2,$$

where the values of r are the electromagnetic form factor radii obtained from Refs. 7-9. The values of the radii used throughout the analysis are:

$$r_p = 0.805\ \text{fm}$$

$$r_\pi = 0.711\ \text{fm}$$

$$r_K = 0.565\ \text{fm}\ .$$

Since the form factors are a small correction to the Coulomb amplitude at small -t, we ignore the experimental uncertainties of the electromagnetic radii. In Eq.(2) the Coulomb phase shift, Ω, is given by West and Yennie[10] as:

$$\Omega = \alpha \ln[\ 1.124\ /\ (\ (b(0) + 4v_p + 4v_a)\ |t|\ )] ,$$

where α is the fine structure constant and b(0) is the nuclear slope at t = 0. We define b(t) below.

Traditionally real part measurements have been analyzed with the nuclear amplitude parametrized as an exponential with a constant slope, B. However, recent results from experiments at Fermilab,[11,12] SLAC,[13] and the ISR[14] show a more complicated t dependence of the nuclear slope. To explore this behavior we employ two parametrizations for the nuclear amplitude and refer to them as the exponential and form factor parametrizations. We define the exponential nuclear amplitude as follows:

$$f_n^e = (\ \sigma_{tot}/4\pi\hbar)\ (i + \rho)\ \exp[\ (Bt + Ct^2)/2\ ] , \qquad (4)$$

where σ_{tot} is the total cross section and where B and C are the constant nuclear slope and curvature. The real and imaginary parts are assumed to have the same functional dependence on t and spin effects are neglected.[15] Thus we define ρ as the ratio of the real to imaginary part of the nuclear amplitude at t = 0.

As we have shown in Ref. 11, the nuclear amplitude can be parametrized by a form suggested in the theoretical models of Chou and Yang[16] and versions of the Additive Quark Model (AQM). These models attribute the major part of the small -t elastic cross section variation to the hadronic form factors of the target and the projectile. These form factors are assumed to be the same as the electromagnetic ones. In the AQM form factors describe the spatial distribution of clothed quarks; in the very small -t region, the scattering is dominated by single quark-quark scattering. Specifically we use the form for the nuclear amplitude suggested by Bialas et. al.[17] and Levin and Shekhter.[18] We define the form factor nuclear amplitude as follows:

$$f_n^{ff} = (\sigma_{tot}/4\pi\hbar)\ (i + \rho)\ G_a(t)\ G_p(t)\ \exp(ut/2)\ , \qquad (5)$$

where σ_{tot}, $G_a(t)$, $G_p(t)$ are defined above and u is the reduced nuclear slope. We discuss below the sensitivity of our results to the precise values of the electromagnetic radii used. In the AQM[19] the radius of the clothed quark is given by $r_q = (2\hbar^2\ u)^{1/2}$. Again we assume the real and imaginary parts have the same functional dependence on t, neglect spin effects, and define ρ to be the ratio of real to imaginary parts.

In summary, we can write the differential cross section as the sum of three terms:

$$d\sigma/dt = \sigma_C + \sigma_I + \sigma_n$$

where σ_C, σ_I, and σ_n are the Coulomb, interference and nuclear contributions. The exponential parametrization of the cross section is given by sum of the three terms below:

$$\sigma_C = (4\pi e^4/c^2)\ G_a^2\ G_p^2\ /\ t^2 \qquad (6a)$$

$$\sigma_I^e = \alpha\ \sigma_{tot}\ G_a\ G_p\ (z_a\rho\ \cos\Omega + \sin\Omega)\ \exp[(Bt+Ct^2)/2]\ /\ t \qquad (6b)$$

$$\sigma_n^e = (\sigma_{tot}^2/16\pi\hbar^2)\ (1 + \rho^2)\ \exp(Bt+Ct^2) \qquad (6c)$$

Similarly the form factor parametrization of the cross section is given by the sum of the three terms below:

$$\sigma_C = (4\pi e^4/c^2)\ G_a^{\ 2}\ G_p^{\ 2}\ /\ t^2 \tag{7a}$$

$$\sigma_I^{\ ff} = \alpha\ \sigma_{tot}\ G_a^{\ 2}\ G_p^{\ 2}\ (z_a\rho\ \cos\Omega + \sin\Omega)\ \exp(ut/2)\ /\ t \tag{7b}$$

$$\sigma_n^{\ ff} = (\ \sigma_{tot}^{\ 2}/16\pi\hbar^2)\ (1 + \rho^2)\ G_a^{\ 2}\ G_p^{\ 2}\ \exp(ut) \tag{7c}$$

In both cases the magnitude and sign of ρ can be determined from the interference term. While the Coulomb term is sharply decreasing ($1/t^2$) and the nuclear term is nearly flat, the interference term is distinguished by a $1/t$ dependence and has its maximum effect on d /dt in the range $0.001 \leq -t \leq 0.003$ $(GeV/c)^2$. However, the accurate determination of ρ requires considerable care in the determination of the nuclear slope in the forward direction. We have paid particular attention to the problem of determining the correct nuclear cross section in the forward direction.

We define the nuclear slope, b(t), and the nuclear curvature, c(t), as follows:

$$b(t) = d[\ \ln \sigma_n\ ]/dt$$

$$c(t) = (1/2)\ \ db/dt\ .$$

Thus for the exponential cross section b and c are:

$$b^e(t) = B - 2C\ |t| \tag{8a}$$

$$c^e(t) = C\ . \tag{8b}$$

For pp the form factor slope and curvature are:

$$b_p^{ff}(t) = u + 8v_p \ (1 + v_p|t|)^{-1} \tag{9a}$$

$$c_p^{ff}(t) = 4v_p^2 \ (1 + v_p|t|)^{-2} \ . \tag{9b}$$

For either πp or Kp the form factor slope and curvature are:

$$b_a^{ff}(t) = u + 4v_a \ (1 + 2v_a|t|)^{-1} + 4v_p \ (1 + v_p|t|)^{-1} \tag{9c}$$

$$c_a^{ff}(t) = 4v_a^2 \ (1 + 2v_a|t|)^{-2} + 2v_p^2 \ (1 + v_p|t|)^{-2} \ . \tag{9d}$$

Dispersion Relations

In 1954 Gell-Mann, Goldberger, and Thirring[20] used causality arguments in the context of quantum electrodynamics to show that the transition amplitudes can be analytically continued to complex values of the energy and to obtain dispersion relations for the amplitude. However, for S-matrix theory it is difficult to rigorously establish the connection between causality and analyticity.[21] S-matrix dispersion relations are thus based on the reasonable assumption of analyticity. In addition crossing symmetry and the optical theorem are used to relate the real part of the scattering amplitude to the integral over the particle and anti-particle total cross sections. However, the contour of integration also includes contributions from pole terms due to intermediate and exchange states and from unphysical cuts along the real axis due to inelastic reactions.

The dispersion relations for πp elastic scattering (by virtue of the pion's spin zero and non-exotic channels) have been proved from axioms of field theory.[22] For pp and Kp elastic scattering, dispersion relations have not been proved in general but have been shown to be valid to all orders in pertubation theory.

For πp scattering the principal pole and unphysical cut contributions are small and well understood, while for Kp and pp they are substantial and have large uncertainties. On a practical level the integration over the total cross sections is made difficult by regions at low energies where the total cross sections have not been measured. At high energies the total cross section varies slowly, while the integral over the total cross sections is sharply peaked. Thus by means of a Taylor series expansion, derivative dispersion relations[23] show that the real part becomes a local function of the total cross section and is insensitive to its value at very high energies.

We compare our results with the calculations of Hendrick et al.,[24] Hohler et al.,[25] and Dumbrajs,[26] and Lipkin.[27] The first three calculations use ananalytic dispersion relations and a detailed fit to total cross section measurements. Hendrick et al. and Hohler et al. extrapolate the total cross sections to very high energies using a $\ln^2(E)$ dependence, while Dumbrajs uses a $[\ln(E)]^{0.967}$ dependence. Lipkin employs derivative dispersion relations[28] and fits the total cross sections at Fermilab energies with a two component Pomeron model. This model gives the total cross section as rising with an $(E)^{0.13}$ dependence.

APPARATUS

The experiment was performed in the M6 West beam line of the Meson Lab at Fermilab. The apparatus, shown in Fig. 1, is a high resolution spectrometer which detects the forward particle. The apparatus is described in detail in Ref. 29; therefore this section will review only the salient features.

The beam line consisted of three stages, each having point to parallel to point focusing (only the latter two stages are shown in Fig. 1). The beam was momentum dispersed at the second focus. There a proportional wire chamber (PWC) with 1 mm wire spacing measured the incident momentum with a precision of 0.05% for $\Delta p/p$ relative to the central beam momentum. The errors and uncertainties quoted in this paper are standard deviations.

Four Cerenkov counters identified pions, kaons, and protons. From the Cerenkov pressure curves, we determined that the contamination of the kaon signal by pions and protons was less than 0.5%. The small contamination of electrons and muons in the beam was tagged at the downstream end of the experiment.

The liquid hydrogen (LH_2) target, 52.7 cm in length, and the PWC's to measure the scattering angle, were located downstream of the Cerenkov counters in the third stage of the beam. The above were mounted on a large reinforced concrete block for stability. Beam defining scintillation counters, B1 and B2 and the veto VH1, were located at the upstream end of the concrete block. Surrounding the target were two u-shaped scintillation counters, RV1 and RV2, with a 1cm thick lead sheet between them. These counters were used to detect converted gamma rays and recoil protons with kinetic energy greater than 250 Mev. We used RV1 and RV2 to help separate inelastic reactions for scatters with -t less than 0.2 $(GeV/c)^2$. Immediately downstream of the target two scintillation counters, VH2 and VH3, were used to suppress unwanted scatters from target electrons and hadronic inelastic scatters. Two stations of high resolution, high pressure PWC's[30] on either side of the LH_2 target (stations 1-4 in Fig. 1) measured the scattering angle. At each station a measurement was made of the track's horizontal (x) and vertical (y) coordinates. In addition station 3 measured the track along the u and v directions (rotated 45 and 135 degrees from the horizontal). The chambers had a 70 μm resolution, and the resulting scattering angles were measured to 30 μrad.

The spectrometer magnets used to determine the momentum of the scattered particle were two dipoles of a type used in the Fermilab main ring. The magnet aperture was nearly rectangular with horizontal and vertical dimensions of 10 and 5 cm. Measurements of the integrated field were made over the magnet aperture; these showed the field to be uniform to 0.04%. A particle with momentum equal to the beam central momentum was bent 34 mrad in the horizontal plane.

A scintillation counter, V, was placed at the third focus, or veto plane, of the beam. Figure 2 shows the placement of this counter relative to the beam center and relative to the projection of the aperture of the last spectrometer magnet onto the veto plane. The beam was focused on the veto, such that the veto would detect unscattered beam tracks. The size of the veto varied with momentum such that scatters with -t less than 0.001 $(GeV/c)^2$ were also vetoed. However primarily because of multiple scattering in the beam line, only about 95% of the beam could be focused on the veto at a given momentum.

At the end of the apparatus were a pair of PWC's with an effective wire spacing of 1 mm. Using these PWC's in conjunction with stations 3 and 4, the outgoing momentum was measured to a precision of 0.1% ($\Delta p/p$) relative to the central momentum.

DATA ACQUISITION

The data collection logic consisted of a two level trigger. The first level used the various scintillation counters to reject quickly 95% of the beam and very small angle scatters. The second level used the high resolution PWC's and an analog calculator called the Hardware Focus Scatter Detector (HFSD)[31] to reject the remaining 5% of the unscattered beam and scatters with -t less than 0.001 $(GeV/c)^2$. An event that satisfied both levels is called a SCATTER.

The first level of the trigger for a SCATTER consisted of the following requirements on the scintillator counters:

1. a reasonable incoming beam trajectory defined by $B1 \cdot B2 \cdot \overline{VHI}$ and other beam defining counters in the second beam stage (not shown in Fig. 1),

2. a unique particle identification by the Cerenkov counters,

3. no other incident particle within ±400 nsec of the trigger,

4. signal from S1 (at the end of the apparatus), and

5. no signal from the veto, V, at the beam third focus.

The second level of trigger was needed since the first level was dominated by the 5% beam halo. The HFSD performed simultaneously two calculations, called HFD and HSD, using the track coordinates as measured in the high resolution PWC's. Figure 3 schematically presents the two calculations. In the HFD test the incoming track, as extrapolated from the coordinates measured in the two high resolution PWC's upstream of the target (stations A and B in Fig. 3), was required to intercept a preset window in the veto plane. This HFD requirement was imposed in both the x and y projections to eliminate beam halo. The HFD test also rejected events with spurious coordinates in the first two stations that would fool the HSD test. The HSD test required that the data from the two upstream and the most downstream high resolution chambers (A, B, and C in Fig. 3) represent the projected angle of a scatter with -t greater than 0.001 $(\mathrm{GeV}/c)^2$. Although the HSD test was made in the vertical and horizontal projections, the second level trigger required that only one projection passed the HSD test. The analog processor took about 5 μsec to make its decision.

Two additional trigger types were recorded along with the scattered events; in neither was the HFSD required. The first additional trigger, called BEAM, was a sample of beam particles that passed the first three requirements of the first level. These triggers provided information for alignment and normalization and the incident phase space for the Monte Carlo simulation.

The second was a specified fraction of events satisfying the first level of the trigger. These events, called PreScaled ACcepted eVenTs (PSACVT), were used to study the HFSD performance and any biases it may have introduced into the data; no such biases were found. In Figs. 4a,b the HSD efficiency in the horizontal projection is shown as a function of q_x (q_x is defined below) at 200 and 70 GeV/c. At 200 GeV/c and $-t$ = 0.0016 $(GeV/c)^2$ the combined HSD efficiency of both projections is better than 99%.

For most of our running the accelerator operated at 300 or 400 GeV with a repetition rate of 10 seconds and a 1 second spill time. The beam contained typically 5×10^5 particles per accelerator pulse. Approximately 400 triggers were recorded per second; out of these 80 were BEAMs and 20 were PSACVTs and the remainder SCATTERs. The relative fraction of events recorded involving a particular particle type (π, K, or p) was scaled to result in apparatus live time of 60%.

Data were also taken with the liquid hydrogen removed from the target assembly. These data were used to subtract the contribution of small angle scatters that occurred outside the liquid hydrogen target, but due to our finite angular resolution were reconstructed inside the target region. The target empty and target full runs were interspersed and taken under the same conditions.

ANALYSIS

Overview

The significant effects of multiple Coulomb scattering and resolution near $t = 0$ suggested that the comparison between data and theory be made by modifying the theory to include the effects of the apparatus. The sum of these corrections is largest at small $-t$ and is between 4 and 6% near $-t = 0.0016$ $(\mathrm{GeV}/c)^2$. These corrections depend strongly on the t dependence of the differential cross section. The three contributions to the differential cross section, σ_C, σ_I, and σ_n, have corrections each with a different functional dependence on t. However, σ_I and σ_n have to be determined from the data. Assuming the theoretical cross sections, Eqs. 6 and 7, the corrections due to multiple scattering in the LH_2 were found analytically. The resolution and acceptance corrections were then included numerically via a Monte Carlo simulation. The corrected theoretical cross sections were then fit to the data. The details of this analysis are found in Ref. 32. Below we provide a brief description.

To facilitate the analysis, the variable q was used:

$$q = (-t)^{1/2} \simeq p_{beam}\, \theta$$

and

$$d\sigma /dq = -2 (-t)^{1/2} \; d\sigma /dt ,$$

where p_{beam} is the incident momentum and θ is the scattering angle. The horizontal and vertical projections of q were called q_x and q_y. There are two major reasons for this choice of variable. First the angular resolution of the apparatus, $\Delta\theta$, is approximately constant as a function of the scattering angle, θ. However the t-resolution of the apparatus is proportional to $\theta\,\Delta\theta$ and thus varies by a factor of 14 over the t range of interest at 200 GeV/c. Since q is proportional to θ, the q-resolution is approximately constant in q and the data could be subdivided in uniform q bins. Secondly, the cross section $d\sigma/dq$ over equal q bins is a more slowly varying function than $d\sigma/dt$ over equal t bins. Thus the binning of $d\sigma/dq$ populates the bins more uniformly. This reduces the sensitivity of the fitting to the integration over the bin and to the migration of events between bins due to resolution and multiple scattering. While the analysis was made using q and $d\sigma/dq$, we present our final results in terms of t and $d\sigma/dt$ for convenience.

Event Reconstruction

The data reduction process kept only events with a single unambiguous track throughout the apparatus. Typically each PWC had one unambiguous coordinate about 95% of the time. However, the lack of redundancy in these PWC's allowed only 50% of all the recorded events to be fully reconstructed.

In the alignment procedure unscattered BEAM events were used to determine the relative spatial position of the PWC's. The PWC's on the block were aligned assuming a straight trajectory, while the PWC's downstream of the spectrometer magnets were aligned assuming no momentum loss. The center of the beam distribution at the second focus PWC was defined to be the central beam momentum. We determined the central value of the beam momentum using the differences between the refractive indices for pions, kaons, and protons in the DISC Cerenkov counter.[33] In Table I the central beam momentum and per cent error used in the analysis are presented.

Several spatial and kinematic quantities were calculated for each reconstructed BEAM or SCATTER event. The incident momentum was determined from the displacement from the beam center in the PWC at the second focus. The high resolution PWC's (stations 1 - 4) were used to measure the scattering angle and the position of the scattering vertex. PWC stations 3, 4, and 6 were used to determine the outgoing momentum and the track position in the veto plane.

BEAM events were also used to determine the q resolution of the apparatus. This resolution is the sum in quadrature of three parts: the PWC angular resolution, the q width of multiple scattering in the LH_2, and the q smearing due to multiple scattering in the PWC's. In Fig. 5a we show the momentum dependence of the q resolution with LH_2 in the target. The multiple scattering contributions are constant as a function of momentum, while the PWC q resolution varies linearly with momentum. By comparing the target full and target empty distributions, the different components can be evaluated. In Shen et al.[34] we reported on measurements of the widths of multiple Coulomb scattering distributions for hydrogen and other nuclei. We find that our measured hydrogen width is in excellent agreement with Moliere's[35] prediction.

The missing mass squared of the undetected recoil particle, m_r^2, is given by:

$$m_r^2 = t + m_p^2 + 2\, m_p\, \Delta E \quad ,$$

where m_p is the mass of the target proton and ΔE is the energy loss. In Fig. 5b, the resolution of the m_r^2 is shown as a function of momentum.

From the reconstructed spatial and kinematic quantities, the position of apertures, the target, and the veto counter, V, were determined and the appropriate cuts selected. A brief description of the most important cuts is given in Table II. These cuts were applied to both the data and Monte Carlo distributions.

Monte Carlo Simulation

A Monte Carlo simulation determined the spatial acceptance of the apertures and the migration of events due to PWC resolution and multiple scattering in the PWC's. The Monte Carlo events were generated using BEAM events to determine the incident phase space. Since we found no significant difference in the phase space of pions, kaons, and protons, the Monte Carlo incident phase space was based on all three particles. Thus only one Monte Carlo distribution at each momentum and beam charge was used.

The polar and azimuthal scattering angles and the longitudinal position of the scattering vertex were generated from a uniform random distribution. Multiple scattering in the PWC's was included as the track was propagated through the apparatus. The PWC spatial resolution was simulated and spatial and kinematic quantities were reconstructed. The same cuts applied to the reconstructed data quantities were also applied to the Monte Carlo reconstructed quantities. In Fig. 6 a typical acceptance is shown as a function of q. At q = 0.040 GeV/c ($-t$ = 0.0016 $(\mathrm{GeV/c})^2$) the acceptance is typically 50% and rapidly rises to a maximum of 75 to 80%. At θ = 1 mrad the vertical apertures of the magnet and PWC stations 4 and 6 combine to sharply decrease the acceptance. At larger angles (θ = 2.5 mrad) the acceptance flattens out between 10 and 15%. The statistical accuracy of the acceptance distributions is less than 0.3% per q-bin and is approximately ten times smaller than the statistical error of the data.

Because of the sharp behaviour of the acceptance, extensive studies and checks were made for systematic effects. The most important of these were detailed comparisons of the data and Monte Carlo distributions of kinematic and spatial quantities. At each energy and beam charge the majority particle's data distributions were compared with the Monte Carlo distributions weighted by the appropriate cross sections. We found that these distribution were in very good agreement.

Target Empty Subtraction

The normalized target full and target empty distributions, N^F and N^{MT}, were obtained as follows:

$$N^F(q_i) = N_{sc}^{\ F}(q_i) \cdot R_s^{\ F} \ / \ N_b^{\ F}$$

$$N^{MT}(q_i) = N_{sc}^{\ MT}(q_i) \cdot R_s^{\ MT} \ / \ N_b^{\ MT} \ ,$$

where $N_{sc}^{\ F}(q_i)$ and $N_{sc}^{\ MT}(q_i)$ are the number of full and empty target, SCATTER events that passed all the cuts and had q in the range $q_i - \Delta q/2 \leq q \leq q_i + \Delta q/2$; $N_b^{\ F}$ and $N_b^{\ MT}$ are the number of full and empty target reconstructed BEAM events. The bin size of the distribution, Δq, varied from 0.002 GeV/c at 70 GeV/c to 0.005 GeV/c at 200 GeV/c. The sampling rate R_s is given by:

$$R_s = N_{s\cdot b} / N_s,$$

where N_s is the total number of reconstructed SCATTER events and $N_{s\cdot b}$ is the total number of reconstructed SCATTER events that are also BEAM events. Typically R_s was 1/225 for target full runs and 1/450 for target empty runs. The ratio, N_b / R_s, is the total incident flux corrected for dead time corrections and absorbtion losses in the apparatus.

The data scattering distribution, $S_D(q_i)$, is given by:

$$S_D(q_i) = (N^F(q_i) - N^{MT}(q_i)) / (D\cdot L\cdot\Delta q),$$

where D is the number of protons per unit volume of LH_2 and L is the target length. The target empty correction N^{MT} is largest at 200 GeV/c where it is 30% of N^F at $-t = 0.0016$ $(GeV/c)^2$, but rapidly decreases to zero at $-t = 0.01$ $(GeV/c)^2$. The statistical error of N^F and N^{MT} are dominated by the statistical errors of R_s^F and R_s^{MT} which are typically 1% and 3% respectively and are independent of t. In summary, $S_D(q_i)$ is the differential cross section for scattering in the liquid hydrogen as measured by our apparatus.

Corrections to Theoretical Cross Section

The theoretical cross sections given by Eqs. 6 and 7 were modified to include the following corrections: multiple scattering, resolution, acceptance, HSD efficiency, and radiative losses.

Since our multiple Coulomb scattering distribution width is in very good agreement with Moliere's prediction, we extend the Moliere formalism to include the interference and nuclear contributions. This transforms the theoretical cross sections of Eqs. 6 and 7 into Moliere distributions, S_{MS}^{e} and S_{MS}^{ff}, due to multiple scattering in the liquid hydrogen. In the t range of interest these distributions are approximated by:

$$S_{MS}^{e} = \sigma_C (1-\varepsilon_C)^{-1} + \sigma_I^{e} (1+\varepsilon_I) + \sigma_n^{e} (1+\varepsilon_n^{e})$$

$$S_{MS}^{ff} = \sigma_C (1-\varepsilon_C)^{-1} + \sigma_I^{ff} (1+\varepsilon_I) + \sigma_n^{ff} (1+\varepsilon_n^{ff}),$$

where ε_C is Bethe's result in Ref. 34 due to pure Coulomb scattering, ε_I is the multiple scattering correction due to the interference term, and ε_n is the double nuclear scattering correction. These corrections are given as follows:

$$\varepsilon_C = (4w^2 / |t|) [1 + .043 \ln(.16 |t| / w^2)]$$

$$\varepsilon_I = (w^2 / |t|) + (1.333 w^4 / t^2)$$

$$\varepsilon_n^{e} = (D L \sigma_{tot}^2 (1+\rho^2)) / (64\pi\hbar^2 b^{e}(0) \exp[(Bt+Ct^2)/2])$$

$$\varepsilon_n^{ff} = (D L \sigma_{tot}^2 (1+\rho^2)) / (64\pi\hbar^2 b^{ff}(0) G_a(t) G_p(t) \exp(-ut/2)) ,$$

where w is the 1/e width of the projected Coulomb multiple scattering Gaussian distribution. D and L, as defined above, are the number of protons per unit volume of LH_2 and the target length. Since L is 52.7 cm, then w is 3.68 MeV/c. At $-t = 0.0016$ $(GeV/c)^2$, ε_C and ε_I are 4% and 1% corrections and rapidly decrease with increasing -t. The double scattering correction, ε_n is less than 1% in our t range. The details of the multiple scattering corrections are found in Ref. 32.

The theoretical cross section corrected for acceptance and resolution, $S_{MS,A,R}(q_i)$, is given by:

$$S_{MS,A,R}(q_i) = \int_{q_i-\Delta q/2}^{q_i+\Delta q/2} dq' \int_0^\infty 2q''dq'' \; S_{MS}(q'') \; R(q'',q')$$

where $R(q'',q')$ is the probability that a scatter generated with $q = q''$ passed all the aperture and kinematic cuts and was reconstructed as a scatter with $q = q'$. The function $R(q'',q')$ is numerically generated by the Monte Carlo. It would be extremely time consuming to evaluate the above integral every time a parameter was changed in the fitting procedure. To avoid this, the cross section, $S_{MS}(q)$ was expanded into a series such that the parameters of the fit are decoupled from q. For the exponential case we write symbolically:

$$S_{MS}{}^e = \sum_j \; g_j{}^e(\rho,\, B,\, C,\, \sigma_{tot}) \; h_j{}^e(q),$$

where g_j is a function only of the parameters to be varied and h_j is a function only of q. In Ref. 32 $g_j{}^e$, $g_j{}^{ff}$, $h_j{}^e$, and $h_j{}^{ff}$ are explicitly defined. We found that a series expansion of 100 terms was sufficiently accurate(1 part in 10^8). The integration over the Monte Carlo events is performed only once and $S_{MS,A,R}(q_i)$ is written as:

$$S_{MS,A,R}(q_i) = \sum_j \; g_j{}^e(\rho,\, B,\, C,\, \sigma_{tot}) \;\; \langle h_j{}^e(q_i)\rangle \; ,$$

where

$$\langle h_j{}^e(q_i)\rangle = \int_{q_i-\Delta q/2}^{q_i+\Delta q/2} dq' \int_0^\infty \; 2q''dq'' \; h_j{}^e(q'') \; R(q'',q').$$

A similar procedure was followed for the form factor cross section.

The theoretical cross section with all our corrections is given by:

$$S_{Th}(q_i) = S_{MS,A,R} \; (1+ \epsilon_{rad}(q_i)) \; / \; E_{HSD}(q_i) \; ,$$

where ϵ_{rad} is the radiative correction and E_{HSD} is the total HSD efficiency. We use the calculations of Sogard[36] to determine the loss of events, ϵ_{rad}, from the elastic peak due to the radiation of photons. In this experiment the correction is significant only for pions; it increases from zero at t = 0 to about 5% at -t = 0.36 $(GeV/c)^2$ for the missing mass squared cut used in the analysis and for the width of the elastic peak. The HSD efficiency, E_{HSD}, is 0.99 at -t = 0.0016 $(GeV/c)^2$ and rapidly becomes 1.0 with increasing -t.

The scintillation counters, RV1, RV2, VH2, and VH3 were used to remove a 2 to 3% non-elastic background. After we applied these cuts, we observed that the inelastic contamination of the elastic peak was less than 1%. No additional correction for inelastic contamination was made.

Fitting Procedure

The fitting procedure consisted of minimizing the following χ^2:

$$\chi^2 = \sum_i (S_D(q_i) - A_n S_{Th}(q_i))^2 / \sigma_i^2 ,$$

where the summation index, i, indicates the i^{th} q-bin; σ_i is the statistical error of $S_D(q_i)$; and A_n is an arbitrary normalization parameter. The χ^2 was minimized by the program MINUIT[37] with the statistical errors on the parameters calculated by the subroutine HESSE.

To remove the effects of multiple scattering, resolution, accepatance, and normalization, the corrected data cross section, $d\sigma^D/dt$, is given by:

$$d\sigma^D/dt = d\sigma/dt\,[S_D(q_i) / (A_n S_{Th}^*(q_i))] ,$$

where $d\sigma/dt$ is the cross section given by Eq. 7 and $S_{Th}^*(q_i)$ is $S_{Th}(q_i)$

evaluated with our final parameters. Because of the extensive length of the corrected cross section tables, we do not publish them here, but do include them in Ref. 32.

RESULTS

The Nuclear Slope

Since the determination of ρ is strongly correlated to the determination of the nuclear slope at small -t, we first discuss the structure of the nuclear cross section. As mentioned above recent experimental results[11-14] have observed substantial deviations from a constant exponential slope for $-t > 0.025$ $(GeV/c)^2$. As we show below, the nuclear curvature, C, is approximately 5 $(GeV/c)^{-4}$ for all six reactions. In the absence of direct experimental evidence below $-t = 0.025$ $(GeV/c)^2$, we assume that this curvature extends down to $t = 0$. Thus even in the small t range, $0.0 \leq -t \leq 0.10$ $(GeV/c)^2$, the variation of the nuclear slope, b(t), is 1 $(GeV/c)^{-2}$ which has a significant effect on the determination of ρ.

The nuclear curvature at large -t is demonstrated in Fig. 7, where $d\sigma/dt$ for pp scattering at 200 GeV/c is shown. The theoretical curve was obtained by fitting the data in the range $0.0016 \leq -t \leq 0.09$ $(GeV/c)^2$ with the exponential cross section Eq. 6 and $C = 0$. We note that the experimental cross section does not decrease as a simple exponential. Similar behaviour is observed for all six reactions between 125 and 200 GeV/c (below 125 GeV/c our t range is too small to observe curvature). By fitting the data with Eq. 6 and allowing B and C to vary, we get a much better representation of the data. In Table III we present B and C for all six reactions at 200 GeV/c. The data were fit in the range $0.01 \leq -t \leq 0.36$ $(GeV/c)^2$ with the exponential cross section Eq. 6 and ρ fixed to our final value (presented in the next section). We see that the values of C are nearly particle independent and are approximately 5 $(\mathrm{GeV}/c)^{-4}$.

However the following considerations suggest that an alternative formulation for the nuclear cross section should be used. We find that our values of B and C depend on the t range of the fit. There is also considerable evidence from other experiments that a constant curvature does not describe the data well.[11-14] In addition our reduced t range at lower momenta does not allow a very accurate simultaneous determination of both B and C, although the values of B and C were consistent with those found at 200 GeV/c.

We found in a related experiment[11] on elastic of pp, π^+p, and π^-p scattering at 200 GeV/c with a high statistical sample in the range $0.025 \leq -t \leq 0.62$ $(\mathrm{GeV}/c)^2$, that the AQM formulation fit the data rather well. Similarly we find with this experiment that the form factor cross section, Eq. 7, with only one free parameter, u, fits very well all six hadronic interactions. We find that the χ^2 's for the form factor fits are comparable to those of the exponential cross section with both B and C free to vary. Also the value of u is insensitive to the t range of the fit.

The local nuclear slope, b(t), provides a mechanism for making a detailed comparison between data and theory. Using the values of u from our final fits at 200 GeV/c (presented in the next section), we calculate the form factor nuclear slope, $b^{ff}(t)$, given by Eq. 9. In Figure 8 we compare $b^{ff}(t)$ to previous measurements of the nuclear slope for pp, π^+p, and π^-p at approximately 200 GeV/c. The slope $b^{ff}(t)$ is shown by the solid line and is extended beyond the t range of our fits by the dotted line. The dashed lines represent the envelope of the uncertainties of the local slopes from fits made to our data using the t intervals employed by Schiz et al. Our results are in rather good agreement with previous measurements.

Our data indicates that the changing curvature is exhibited by all six reactions from 100 to 200 GeV/c. In Figures 9a-f we compare the form factor slope, $b^{ff}(t)$, with the exponential parametrization of the nuclear slope, $b^{e}(t)$, of Ayres et al.[12] and Akerlof et al.[12] at -t = 0.1 and 0.2 $(GeV/c)^2$. We note the excellent agreement of the local slopes at -t = 0.2 $(GeV/c)^2$. At -t = 0.1 $(GeV/c)^2$ our local slopes are substantially higher than the values of Ayres et al. and Akerlof et al., indicating that the curvature is increasing with decreasing -t for all six reactions.

The form factor cross section provides an elegant explanation for the large curvature that we measure at low -t and the small curvature that Ayres et al. and Akerlof et al. measure at higher -t. For instance, in pp scattering the form factor curvature, $c^{ff}(t)$, equals 4.9 $(GeV/c)^{-4}$ at t = 0.2 $(GeV/c)^2$, which is good agreement with C = 5 $(GeV/c)^{-4}$. At t = 0.4 $(GeV/c)^2$, the curvature has decreased to $c^{ff}(t)$ = 2.3 $(GeV/c)^{-4}$ which is in good agreement with previous measurements[12] of C in this t range. Calculating $c^{ff}(t)$ for other reactions, we see that the curvature is almost particle and momentum independent. This is also in good agreement with previous measurements.

Because of the short lever arm and low statistics at large -t of this data, we are unable to fit for the nuclear form factor radii.

However in our previous result[11], we were able to fit for the proton and pion nuclear radii. The fits tended to give values of proton radius 7% smaller than the electromagnetic values, while the pion radius was consistent with the electromagnetic measurements. For kaons we have no such independent check and only one experimental measure of the kaon radius.[9] To first order our values of ρ are insensitive to small changes in the radii, since the values of u will vary to compensate.

To illustrate the stability of the form factor fits, the data at 200 GeV/c were fit with the form factor cross section in the intervals $0.0016 \leq -t \leq -t_{max}$. To contrast our sensitivity fits were also made with the exponential cross section with C = 0. For both types of fits the values of $-t_{max}$ ranged from 0.05 to 0.36 $(GeV/c)^2$. In Fig. 10a the fitted values of B and u are plotted as a function of $-t_{max}$ for all six reactions at 200 GeV/c. For convenience B and u are superimposed and a dashed line goes through the value of u from our final fits. We note as the range of the fit increased B decreased, while u remained constant within statistical errors. The χ^2 per degree of freedom also rapidly increased for the exponential case but remained near one for the form factor case. Since ρ is strongly correlated to the nuclear slope, the variation of ρ follows the variation of B and u. In addition the variations of ρ for particle and anti-particle will be reversed. This behaviour is shown in Fig. 10b, where a dashed line goes through the value of ρ from our final fits. For small $-t_{max}$ the values of ρ for both formulations converge, although with large uncertainties. At lower momenta the same behaviour is noted, but over reduced t ranges. Results of fits to the data with the exponential cross section and C fixed to the values of Table 3 are similar to those with the form factor, but with slightly larger variations of ρ and B as a function of $-t_{max}$.

In summary, we choose the form factor cross section, Eq. 7, since it gives a good representation of the data and makes the determination of ρ less sensitive to the fitting range. A fit over a larger t interval increases the statistical certainty in ρ by increasing the certainty in the slope parameter.

The Real Parts

In Tables IV-IX we present the results of fitting the data with the form factor cross section over the indicated t ranges. The parameters ρ, u and A_n were allowed to vary except at 70 Gev/c, where u was held constant. The value of u at 70 GeV/c was determined by fitting the values of u from higher momenta to the logarithmic function u_f given by

$$u_f = a + b \ln(p_{beam}).$$

The total cross section, σ_{tot}, was held fixed to the values of Carroll et al.[38]

In Figs. 11a-f the corrected data and form factor cross sections are compared over the full t range for all six particles at all six momenta. In Figs. 12a-f we compare the data and form factor cross sections divided by the form factor cross section with $\rho = 0$ over the fitting interval.

Systematics

Studies were made to determined the sensitivity of the results to variations of the more important cuts. Each of the first five cuts in

Table 2 were made significantly more restrictive and were applied one at a time to both data and Monte Carlo distributions. New fits were made for all particles at all energies; the resulting values of ρ, u, and A_n were all within the statistical errors of our final results. We emphasize that the data for three particles of like charge at a given momentum had the same cuts applied. In addition only the veto cut varied significantly between momenta due to the changing veto size.

We believe that the normalization parameter, A_n, was needed to compensate for losses of BEAM events due to PWC inefficiencies. Although the Monte Carlo simulated the t dependent effects of these inefficiencies (Cut 6 in Table 2), we had no reliable way of estimating these effects on the overall normalization. We expect that the values of A_n should then be the same for all three particles taken simultaneously. In Tables 3 and 4 we see that the values of A_n are in good agreement for the like charge particles at a given momentum. At 200 GeV/c the beam area was smallest and thus more sensitive to these corrections.

Measurements were also made at 100 GeV/c with negative charge particles. But because of problems during the data acquisition, we have not included them in our results.

In the fitting procedure we found that the statistical errors on ρ, u and A_n are symmetric and parabolic and that the χ^2 contours are smooth and ellipsoidal. The dependence of ρ, u, and A_n on each other and other quantities are given by the derivatives in Tables IV-IX. The derivatives $d\rho/du$, $d\rho/dA_n$, and du/dA_n were determined by fixing the parameter in the denominator to a different value and allowing the other two parameters to vary. The derivatives with respect to other quantities were determined by allowing all three parameters to vary. We note that $(d\rho/du)\ \sigma_u$ and $(d\rho/dA_n)\ \sigma_{A_n}$ comprise about half of the statistical error of ρ. Since the total cross sections have uncertainties between 0.1 to 0.25%, they contribute very little to the systematic error. The main contributions to the systematic errors come from the uncertainty of the absolute momentum ($\Delta p/p$ was about 0.3%) and the uncertainty of the target empty subtraction (about 3.0%). The largest error to ρ from the momentum uncertainty occurs at 70 GeV/c where it is 0.008. The largest error on ρ due to the target empty subtraction is 0.008 at 200 GeV/c. Typically the two errors add in quadrature to a 0.01 error in ρ. We believe the systematic errors are point to point, rather than scale shifts and are added quadratically with our statistical errors to give the total error. The statistical, systematic, and total errors for ρ and u are also included in Tables IV-IX.

DISCUSSION

In Figs. 13a-f we compare our values of ρ for all six reactions with previous measurements and various dispersion relation predictions. For π^+p the values of ρ are quite consistent with the predictions of of Hendrick et. al. and of Hohler et al., while those of Lipkin are slightly low. However for π^-p the values of ρ are more consistent with Lipkin, while those of Hendrick and Hohler seem a little high. For K^+p and K^-p the predictions of Hendrick et. al. and Lipkin fit the data well, while the results of Dumbrajs are somewhat low. The predictions of Lipkin and Hendrick et. al. are in very good agreement with the $\bar{p}p$ real parts.

Our pp results are higher than dispersion predictions and previous experimental results. We believe that this is due to the steeper slope we have measured in the forward direction. In order to verify this, we fit the data of Jenkins et al.[1] with the form factor cross section. Since their t range is severely limited, we use the values of u given by the function u_f (Eq. 10). In Table X we present the results of the fits, in which the χ^2's are as good as with their exponential fits. In Fig. 14 we have plotted the refitted real parts of Jenkins et al. and see that they are in good agreement with our results.

On the other hand, we can fit our data at 200 GeV/c using the exponential cross section and Jenkins' slope, $B = 11.56 \pm 0.12$ (GeV/c)$^{-2}$. Our values of ρ are then consistent with their published results, but only if we use the limited t range, $0.0016 \leq -t \leq 0.04$ (GeV/c)^2. If we extend the range of our fit to $-t_{max} = 0.09$ (GeV/c)^2, the steep fall off of our data forces ρ to be inconsistent. The slopes that Jenkins et al. uses comes from a logarithmic fit to a previous measurement[39] made in the range $0.005 < -t < 0.09$ (GeV/c)^2. To compare slopes we fit our data with the exponential cross section and $C = 0.0$ (GeV/c)$^{-4}$ and $-t_{max} = 0.09$ (GeV/c)^2. We obtain $B = 12.24 \pm 0.17$ (GeV/c)$^{-2}$, which still leaves a discrepancy in the slope of 0.73 (GeV/c)$^{-2}$.

CONCLUSIONS

We find that the real parts for $\bar{p}p$, π^+p, π^-p, K^+p, and K^-p are in good agreement with dispersion relations. The real parts for pp, however, are higher than dispersion relations and indicate that ρ_{pp} goes through zero near 175 GeV/c. Hendrick et al. point out that the contributions from pole terms and unphysical cuts for pp and $\bar{p}p$ scattering are still significant at these energies. Since the contributions are the same for both reactions, it is then puzzling to have such good agreement between our $\bar{p}p$ results and the dispersion relations of Hendrick et al. and Lipkin.

As derivative dispersion relations show, the real part at high energies becomes a local function of the total cross section. Specifically the real part is strongly correlated to the first derivative of the total cross section with respect to energy. This is reflected the in the similarity of the different computations of dispersion relations even when they differ in their extrapolations to higher energies. Our results are consistent with increasing total cross sections for all six reactions. In particular following the cross section predictions of Lipkin, we expect the $\bar{p}p$ total cross section to start increasing in the neighborhood of 300 GeV/c.

ACKNOWLEDGMENTS

We would like to thank the following persons for their valuable contributions: Peter Martin, Adrian Disco, Satish Dhawan, William Frieze, Irving Winters, Jon Blomquist, Garvie Hale, and Ed Steigmeyer. We also thank the staff of Fermilab for their helpful efforts. This work was supported in part by the U.S. Department of Energy. One of us (L.R.) was a fellow of the Swiss National Fund for Scientific Research and a second member (L.A.F.) was supported in part by a Ford Foundation Doctoral Fellowship for Mexican-Americans and Puerto Ricans.

REFERENCES

[a]Present address: Lawrence Berkeley Laboratory
Berkeley, California 94720

[b]Present address: CERN, Geneva, Switzerland

[c]Present address: Bell Laboratories
Holmdel, New Jersey 07733

[d]Visitor from: Rutherford Laboratory, Chilton,
Didcot, Berkshire, England

[e]Present address: SLAC, P.O. Box 4349
Stanford, California 94035

[f]Present address: Brookhaven National Laboratory
Upton, New York 11973

[g]Present address: Arthur Young and Company
One IBM Plaza, Chicago, Illinois 60611

[1]Real part measurements for pp scattering:

A. A. Vorobyov et al., Phys. Lett. 41B, 639 (1972).

P. Jenni et al., Nucl. Phys. B129, 232 (1977);

K. J. Foley et al., Phys. Rev. Lett. 19 (1967);

V. D. Apokin et al., Sov. J. Nucl. Phys. 25, 51 (1977);

E. Jenkins et al., Fermilab Pub. 78/35-EXP (1978); Submitted to Sov. J. Nucl. Phys.; also published as D. Gross et al., Phys. Rev. Lett. 41, 217 (1978);

U. Amaldi et al., Phys. Lett. 43B, 231 (1973);

U. Amaldi et al., Phys. Lett. 66B, 390 (1977).

[2]Real part measurements for π^-p scattering:

P. Baillon et al., CERN 75-10 (1975); also published in Nucl. Phys. B105, 365 (1976)

K. J. Foley et al., Phys. Rev. 181, 1775 (1969);

V. D. Apokin et al., Phys. Lett. 56B, 391 (1975);

J. P. Burq et al., Phys. Lett. 77B, 438 (1978);

J. P. Burq et al., CERN EP Internal Report, 78-07.

[3]Real part measurements for π^+p scattering:

P. Baillon et al., CERN 75-10;

K. J. Foley et al., Phys. Rev. 181, 1775 (1969);

V. D. Apokin et al., Sov. J. Nucl. Phys. 25, 51 (1977).

[4]Real part measurements for K^+p scattering;

P. Baillon et al., CERN 75-10;

P. Baillon et al., Nucl. Phys. B107, 189 (1976);

R. K. Carnegie et al., Phys. Lett. 59B, 308 (1975);

V. D. Apokin et al., Sov. J. Nucl. Phys. 25, 51 (1977).

[5]Real part measurements for K^-p scattering:

P. Baillon et al., CERN 75-10;

P. Baillon et al., Nucl. Phys. B107, 189 (1976);

J. R. Campbell et al., Nucl. Phys. B64, 1 (1973);

R. K. Carnegie et al., Phys. Lett. 59B, 308 (1975);

R. J. Deboer et al., Nucl. Phys. B106, 125 (1976);

R. W. Meijer, Thesis, Amsterdam University, 1973.

[6]Real Part measurements for $\bar{p}p$ scattering:

P. Jenni et al., Nucl. Phys. B94, 1 (1975);

P. Jenni et al., Nucl. Phys. B129, 232 (1977);

D. W. S. Leith et al., private communication;

K. J. Foley et al., Phys. Rev. Lett. 19, 857 (1967).

[7]L. N. Hand et al., Rev. Mod. Phys. 35, 335 (1963).

[8]A. Quenzer et al., Phys. Lett. 76B, 512 (1978) and the references therein.

[9]E. Dally et al., submitted to XIX International Conference on High Energy Physics, Tokyo, August, 1975.

[10]G. B. West and D. R. Yennie, Phys. Rev. 172, 1413 (1968).

[11]A. Schiz et al., submitted to Phys. Rev.

[12]C. W. Akerlof et al., Phys. Rev. D14, 2864 (1976);

D. S. Ayres et al., Phys. Rev. D15, 3105 (1977).

[13]R. K. Carnegie et al., Phys. Lett. 59B, 313 (1972).

[14]G. Barbiellini et al., Phys. Lett. 39B, 663 (1972);

J. P. Burq et al., Phys. Lett. 77B, 438 (1978).

[15]H. A. Bethe, Ann. Phys. 3, 190 (1958); In Ref. 1 Amaldi(1973) discusses the bases for ignoring spin effects at high energies.

[16]T. T. Chou and C. N. Yang, Phys. Rev. 170, 1591 (1968).

[17]A. Bialas et al., Acta Phys. Pol. 8B, 855 (1977);

N. W. Dean, Phys. Rev. 1D, 2703 (1970).

[18]J. J. J. Kokkedee and L. Van Hove, Nouvo Cim. 42, 711 (1966);

E. M. Levin and V. M. Shekhter, Leningrad Nuclear Physics Institute Preprint, "Small-Angle Elastic Scattering and Quark

Model", 1978; Ya. I. Azimov et al., Proc. of the IXth Winter LPNJ School on Nuclear Physics and Elementary Particles (Leningrad 1974), translated in CERN Trans. 74-8.

[9]The quark-quark scattering amplitude is written in impact parameter space (b-space) as $\exp(-b^2/r_q^2)$; private communication, H. Miettenen. A similar parametrization is used in Ref. 17.

[20]M. Gell-Mann et al., Phys. Rev. 95, 1621 (1954).

[21]R. J. Eden, P. V. Landshoff, D. I. Olive, and J. C. Polkinghorne, "The Analytic S-Matrix", pp 3, 16 (Cambridge University Press, London and New York, 1966).

[22]A. Martin, Nuovo Cimento 42, 930 (1966); 44, 1219 (1966).

[23]J. B. Bronzan et al., Phys. Lett. 49B, 272 (1974).

[24]R. E. Hendrick and B. Lautrup, Phys. Rev. D11, 529 (1975); T. R. Englemann and R. E. Hendrick, Phys. Rev. D16, 2891 (1977). R. E. Hendrick provided a numerical tabulation of his results for which we are grateful.

[25]G. Hohler et al., Kernforschungzentrum Karlsruhe, KFK 2457, April, 1977.

[26]O. Dumbrajs, University of Helsinki, HU-TFT-78-15, April, 1978.

[27]H. J. Lipkin, Phys. Rev. D17, 366 (1978).

[28]R. J. Eden, "High Energy Collisions of Elementary Particles," (Cambridge University Press, London, 1967), p. 194.

[29]A. Schiz, Thesis, Yale University, 1979; also A. J. Slaughter et al., to be published.

[30]W. Frieze et al., Nucl. Instrum. Methods 136, 93 (1976).

[31]S. Dhawan and R. D. Majka, "A Hardware Scatter Detector," IEEE

Transactions on Nuclear Science, Vol. NS-22 (1975).

[32] L. A. Fajardo, Thesis, Yale University, 1980.

[33] M. Benot et al., Nucl. Instrum. Methods 105, 431 (1972).

[34] G. Shen et al., Phys. Rev. D, 20, 1584 (1979).

[35] G. Moliere, Z. Naturforsch. 3a, 78 (1953);
H. A. Bethe, Phys. Rev. 89, 1256 (1953).

[36] M. Sogard, Phys. Rev. D9, 1486 (1974).

[37] F. James and M. Roos, CERN Computer 7600 Interim Program Library, D506 and D516.

[38] A. S. Carroll et al., Phys. Rev. Lett. 33, 932 (1974).

[39] V. Bartenev et al., Phys. Rev. Lett. 31, 1088 (1973).

[40] R. Schamberger, Jr. et al., Phys. Rev. D17, 1268 (1978).

TABLE I

Momenta Used in the Analysis

Nominal Momentum (GeV/c)	Beam Momentum (GeV/c)	Momentum Uncertainty ($\Delta p/p$)
70	70.00	0.0036
100	100.00	0.0030
125	124.77	0.0016
150	151.44	0.0033
175	174.33	0.0037
200	200.80	0.0038

TABLE II

Principal Cuts Used in the Analysis

Cut No.	Description
1	The limiting aperture of the high resolution PWC's was the sensitive area of station 4. Tracks were required to be within its reduced area.
2	The spectrometer magnet channel cross section was a rectangle with rounded corners as shown in Fig. 2. The limiting aperture of the spectrometer magnets was its most downstream exit. Tracks were required to be within its reduced area.
3	Tracks in the veto plane were required to be outside an enlarged veto region. See Fig. 2.
4	The longitudinal position of the interaction vetex was required to be within the target region.
5	The recoil mass squared, m_r^2, as defined in the text was required to be in the neighborhood of the proton mass squared.
6	Since stations 1 and 2 defined the incident beam phase space, an inefficient or inactive PWC area was of no consequence. In station 3 the redundancy of x, y, u, and v measurements made such inefficiencies negligible. However in station 4 there is no redundancy and tracks were required to be outside of inefficient or inactive areas.
7	The final aperture of the apparatus was station 6. All tracks were required to be within its sensitive area.

TABLE III

Exponential Fit[a] at 200 GeV/c

Parameter	Reaction					
	pp	π^+p	K^+p	$\bar{p}p$	π^-p	K^-p
B $(GeV/c)^{-2}$	12.64 ± 0.12	10.72 ± 0.15	9.60 ± 0.22	13.27 ± 0.24	10.85 ± 0.14	9.51 ± 0.19
C $(GeV/c)^{-4}$	5.06 ± 0.44	6.08 ± 0.54	4.37 ± 0.79	4.54 ± 0.97	5.87 ± 0.51	3.38 ± 0.69
A_n	1.10 ± 0.01	1.11 ± 0.01	1.10 ± 0.01	1.10 ± 0.01	1.11 ± 0.01	1.05 ± 0.01
χ^2/DF[b]	1.09	1.57	1.19	1.07	0.86	1.18

[a]The range of the fit was $0.01 \leq -t \leq 0.36\ (GeV/c)^2$

[b]The number of degrees of freedom, DF, was 97 for all six fits.

LEGEND FOR TABLES IV-IX

Acronym	Description[a]	Units
MOMENTUM	p_{beam}	GeV/c
RHO	ρ ± total error	--
RSTAT,RSYS	statistical,systematic errors on ρ	--
U	u ± total error	$(GeV/c)^{-2}$
USTAT,USYS	statistical,systematic errors on u	$(GeV/c)^{-2}$
AN	A_n	--
SIGT	σ_{tot}	mb
CHI/D.F.	χ^2/degrees of freedom	--
D.F.	degrees of freedom	--
EVENTS (K)	number of events in thousands	--
MPTYERR	$\Delta R_s^{MT}/R_s^{MT}$	--
DR/DU	$d\rho/du$	$(GeV/c)^2$
DR/DAN	$d\rho/dA_n$	--
DR/DMPTY	$R_s^{MT}(d\rho/dR_s^{MT})$	--
DR/DSIGT	$d\rho/d\sigma_{tot}$	mb^{-1}
DR/DRA	$d\rho/dr_a$	fm^{-1}
DR/DRP	$d\rho/dr_p$	fm^{-1}
DR/DCMOM	$p_{beam}(d\rho/dp_{beam})$	--
DU/DAN	du/dA_n	$(GeV/c)^{-2}$
DU/DMPTY	$R_s^{MT}(du/dR_s^{MT})$	$(GeV/c)^{-2}$
DU/DSIGT	$du/d\sigma_{tot}$	$(GeV/c)^{-2}\ mb^{-1}$
DU/DRA	du/dr_a	$(GeV/c)^{-2}\ fm^{-1}$
DU/DRP	du/dr_p	$(GeV/c)^{-2}\ fm^{-1}$
DU/DCMOM	$p_{beam}(du/dp_{beam})$	$(GeV/c)^{-2}$
DAN/DMPTY	$R_s^{MT}(dA_n/dR_s^{MT})$	--
DAN/DSIGT	$dA_n/d\sigma_{tot}$	mb^{-1}
DAN/DRA	dA_n/dr_a	fm^{-1}
DAN/DRP	dA_n/dr_p	fm^{-1}
DAN/DCMOM	$p_{beam}(dA_n/dp_{beam})$	--
TMIN,TMAX	$-t_{min},-t_{max}$	$(GeV/c)^2$

[a]The parameters are defined as follows: ρ, u, σ_{tot} in Eq. 7; r_a, r_p in Eq. 3; R_s and A_n in the Analysis Section.

TABLE IV

RESULTS FOR pp SCATTERING

MOMENTUM	70	100	125	150	175	200
RHO	-0.115±0.015	-0.074±0.018	-0.024±0.014	0.008±0.012	-0.011±0.019	0.019±0.016
RSTAT,RSYS	0.013 0.008	0.016 0.007	0.013 0.005	0.010 0.006	0.017 0.007	0.014 0.009
U	0.460 --	1.035±0.142	1.247±0.092	1.369±0.059	1.539±0.087	1.839±0.049
USTAT,USYS	-- --	0.141 0.018	0.092 0.006	0.059 0.007	0.087 0.007	0.048 0.004
AN	1.006±0.008	1.037±0.011	1.031±0.007	1.035±0.005	1.038±0.008	1.106±0.005
SIGT	38.280	38.460	38.600	38.690	38.850	38.970
CHI/D.F.	0.703	1.003	0.769	1.065	1.150	1.015
D.F.	104	124	120	137	92	112
EVENTS (K)	157	178	229	385	124	282
NPTYERR	0.043	0.035	0.037	0.036	0.030	0.031
DR/DU	0.056	0.083	0.093	0.105	0.116	0.149
DR/DAN	1.436	1.300	1.455	1.534	1.588	1.471
DR/DNPTY	0.069	0.065	0.094	0.107	0.119	0.246
DR/DSIGT	-0.026	-0.029	-0.024	-0.020	-0.020	-0.016
DR/DRA	--	--	--	--	--	--
DR/DRP	1.366	0.100	0.145	0.202	0.274	0.465
DR/DCMOM	-2.068	-2.284	-1.881	-1.526	-1.568	-1.263
DU/DAN	--	11.247	11.029	10.653	9.357	8.087
DU/DNPTY	--	-0.259	-0.088	-0.012	0.027	0.060
DU/DSIGT	--	-0.073	-0.046	-0.029	-0.024	-0.013
DU/DRA	--	--	--	--	--	--
DU/DRP	--	-23.772	-22.885	-22.064	-21.405	-19.905
DU/DCMOM	--	-5.321	-3.383	-2.148	-1.836	-1.031
DAN/DNPTY	0.003	-0.019	-0.011	-0.010	0.000	-0.005
DAN/DSIGT	-0.062	-0.066	-0.060	-0.057	-0.058	-0.059
DAN/DRA	--	--	--	--	--	--
DAN/DRP	1.271	0.118	0.146	0.177	0.231	0.335
DAN/DCMOM	-1.802	-1.990	-1.586	-1.334	-1.395	-1.274
TMIN,TMAX	0.0018 0.0625	0.0016 0.1225	0.0015 0.1592	0.0015 0.2025	0.0016 0.2500	0.0016 0.3600

TABLE V

RESULTS FOR π^+p SCATTERING

MOMENTUM	70	100	125	150	175	200
RHO	-0.025±0.016	-0.003±0.020	0.052±0.014	0.058±0.014	0.035±0.018	0.053±0.017
RSTAT,RSYS	0.012 0.010	0.018 0.009	0.013 0.005	0.011 0.008	0.015 0.009	0.014 0.009
U	0.300 --	0.505±0.200	0.870±0.120	0.867±0.084	0.970±0.097	1.152±0.062
USTAT,USYS	-- --	0.198 0.026	0.119 0.011	0.083 0.013	0.096 0.012	0.062 0.007
AN	1.021±0.008	1.041±0.014	1.054±0.009	1.048±0.007	1.044±0.009	1.103±0.007
SIGT	23.220	23.330	23.430	23.500	23.710	23.840
CHI/D.F.	0.736	1.009	0.930	0.986	1.260	1.549
D.F.	104	124	120	137	92	112
EVENTS (K)	107	120	147	187	100	144
MPTYERR	0.051	0.035	0.037	0.039	0.029	0.031
DR/DU	0.048	0.075	0.079	0.091	0.106	0.131
DR/DAN	1.247	1.162	1.218	1.282	1.328	1.256
DR/DMPTY	0.059	0.064	0.062	0.094	0.100	0.193
DR/DSIGT	-0.055	-0.064	-0.053	-0.047	-0.047	-0.038
DR/DRA	0.509	0.064	0.080	0.111	0.158	0.234
DR/DRP	0.592	0.044	0.059	0.087	0.128	0.202
DR/DCHOM	-2.609	-2.992	-2.505	-2.159	-2.223	-1.777
DU/DAN	--	12.835	12.178	10.958	9.392	7.677
DU/DMPTY	--	-0.224	-0.172	0.008	0.038	0.049
DU/DSIGT	--	-0.208	-0.138	-0.093	-0.074	-0.041
DU/DRA	--	-9.495	-9.016	-8.538	-8.090	-7.337
DU/DRP	--	-11.756	-11.340	-10.912	-10.503	-9.776
DU/DCHOM	--	-8.279	-5.940	-4.061	-3.314	-1.855
DAN/DMPTY	-0.009	-0.025	-0.030	-0.014	-0.006	-0.015
DAN/DSIGT	-0.103	-0.113	-0.103	-0.098	-0.098	-0.097
DAN/DRA	0.506	0.080	0.092	0.113	0.151	0.208
DAN/DRP	0.587	0.064	0.075	0.094	0.128	0.183
DAN/DCHOM	-1.831	-2.196	-1.732	-1.508	-1.571	-1.370
TMIN,TMAX	0.0018 0.0625	0.0016 0.1225	0.0015 0.1592	0.0015 0.2025	0.0016 0.2500	0.0016 0.3600

TABLE VI

RESULTS FOR K^+p SCATTERING

MOMENTUM	70	100	125	150	175	200
RHO	0.013±0.026	0.065±0.026	0.061±0.023	0.067±0.021	0.029±0.024	0.071±0.021
RSTAT,RSYS	0.023 0.011	0.025 0.009	0.023 0.005	0.020 0.009	0.022 0.009	0.019 0.009
U	0.400 --	1.291±0.309	1.070±0.219	1.209±0.155	1.246±0.140	1.784±0.090
USTAT,USYS	-- --	0.308 0.022	0.218 0.010	0.154 0.015	0.139 0.012	0.089 0.009
AN	0.998±0.017	1.068±0.021	1.026±0.016	1.043±0.013	1.005±0.014	1.096±0.010
SIGT	18.520	18.880	19.180	19.360	19.680	19.900
CHI/D.F.	0.807	0.928	1.316	0.865	1.272	1.301
D.F.	104	124	120	137	92	112
EVENTS (K)	25	51	45	54	44	64
MPTYERR	0.041	0.035	0.038	0.040	0.030	0.031
DR/DU	0.018	0.067	0.081	0.091	0.108	0.125
DR/DAN	1.217	1.102	1.215	1.241	1.317	1.200
DR/DMPTY	0.056	0.050	0.067	0.077	0.086	0.162
DR/DSIGT	-0.083	-0.078	-0.073	-0.063	-0.061	-0.051
DR/DRA	0.382	0.015	0.029	0.045	0.067	0.104
DR/DRP	0.588	0.034	0.059	0.088	0.128	0.191
DR/DCMOM	-3.080	-2.821	-2.728	-2.408	-2.395	-1.996
DU/DAN	--	14.071	12.095	10.713	8.872	7.652
DU/DMPTY	--	-0.332	-0.108	-0.073	-0.033	0.071
DU/DSIGT	--	-0.217	-0.171	-0.129	-0.088	-0.059
DU/DRA	--	-7.695	-7.445	-7.201	-6.966	-6.567
DU/DRP	--	-11.736	-11.276	-10.834	-10.415	-9.715
DU/DCMOM	--	-6.245	-5.582	-4.494	-3.122	-2.196
DAN/DMPTY	-0.009	-0.041	-0.024	-0.023	-0.013	-0.016
DAN/DSIGT	-0.126	-0.132	-0.123	-0.120	-0.115	-0.116
DAN/DRA	0.366	0.031	0.042	0.055	0.073	0.102
DAN/DRP	0.565	0.059	0.078	0.102	0.135	0.185
DAN/DCMOM	-1.810	-1.796	-1.714	-1.584	-1.594	-1.405
TMIN,TMAX	0.0018 0.0625	0.0016 0.1225	0.0015 0.1592	0.0015 0.2025	0.0016 0.2500	0.0016 0.3600

TABLE VII

RESULTS FOR $\bar{p}p$ SCATTERING

MOMENTUM	70	125	150	175	200
RHO	0.010±0.018	0.012±0.020	-0.001±0.028	0.067±0.039	0.029±0.030
RSTAT,RSYS	0.017 0.006	0.019 0.006	0.027 0.005	0.038 0.007	0.028 0.011
U	2.080 --	2.370±0.139	2.427±0.160	2.942±0.187	2.591±0.097
USTAT,USYS	-- --	0.138 0.011	0.160 0.007	0.187 0.006	0.097 0.004
AN	0.944±0.008	1.062±0.011	1.026±0.013	1.016±0.020	1.112±0.012
SIGT	43.050	41.710	41.790	41.650	41.440
CHI/D.F.	1.252	0.995	0.952	1.025	1.068
D.F.	104	120	137	92	112
EVENTS (K)	58	95	48	31	72
MPTYERR	0.064	0.042	0.054	0.031	0.030
DR/DU	-0.045	-0.087	-0.100	-0.119	-0.151
DR/DAN	-1.584	-1.455	-1.608	-1.658	-1.723
DR/DMPTY	-0.052	-0.073	-0.088	-0.120	-0.108
DR/DSIGT	0.017	0.021	0.017	0.020	0.017
DR/DRA	--	--	--	--	--
DR/DRP	-1.116	-0.137	-0.198	-0.268	-0.448
DR/DCMOM	1.464	1.727	1.435	1.688	1.358
DU/DAN	--	11.655	11.324	8.239	7.214
DU/DMPTY	--	-0.147	-0.123	0.012	0.022
DU/DSIGT	--	-0.039	-0.024	-0.023	-0.012
DU/DRA	--	--	--	--	--
DU/DRP	--	-22.984	-22.205	-21.811	-20.310
DU/DCMOM	--	-3.147	-1.977	-1.867	-1.043
DAN/DMPTY	-0.014	-0.019	-0.018	0.015	0.022
DAN/DSIGT	-0.047	-0.056	-0.052	-0.055	-0.057
DAN/DRA	--	--	--	--	--
DAN/DRP	0.866	0.138	0.167	0.234	0.351
DAN/DCMOM	-1.205	-1.531	-1.303	-1.549	-1.420
THIN,TMAX	0.0018 0.0625	0.0015 0.1592	0.0015 0.2025	0.0016 0.2500	0.0016 0.3600

TABLE VIII

RESULTS FOR $\pi^- p$ SCATTERING

MOMENTUM	70	125	150	175	200
RHO	0.027±0.016	0.035±0.017	0.027±0.018	0.054±0.016	0.064±0.020
RSTAT,RSYS	0.013 0.010	0.015 0.009	0.017 0.007	0.013 0.009	0.017 0.012
U	0.310 --	0.868±0.115	1.033±0.102	1.306±0.071	1.331±0.060
USTAT,USYS	-- --	0.114 0.016	0.102 0.006	0.071 0.010	0.059 0.007
AN	0.934±0.008	1.066±0.011	1.058±0.011	1.030±0.009	1.105±0.010
SIGT	24.000	24.070	24.110	24.230	24.330
CHI/D.F.	1.106	1.015	0.958	1.270	0.973
D.F.	104	120	137	92	112
EVENTS (K)	107	175	141	216	137
MPTYERR	0.063	0.041	0.052	0.024	0.028
DR/DU	-0.048	-0.098	-0.112	-0.126	-0.172
DR/DAN	-1.394	-1.211	-1.319	-1.351	-1.433
DR/DMPTY	-0.055	-0.066	-0.100	-0.091	-0.296
DR/DSIGT	0.051	0.057	0.050	0.051	0.045
DR/DRA	-0.521	-0.104	-0.145	-0.186	-0.314
DR/DRP	-0.606	-0.079	-0.116	-0.153	-0.273
DR/DCMOM	2.467	2.761	2.396	2.517	2.197
DU/DAN	--	9.361	8.451	7.291	5.125
DU/DMPTY	--	-0.133	-0.009	0.004	0.108
DU/DSIGT	--	-0.117	-0.081	-0.068	-0.038
DU/DRA	--	-8.963	-8.463	-8.142	-7.285
DU/DRP	--	-11.296	-10.849	-10.551	-9.734
DU/DCMOM	--	-4.913	-3.538	-2.998	-1.730
DAN/DMPTY	-0.010	-0.015	0.000	0.006	0.055
DAN/DSIGT	-0.090	-0.109	-0.104	-0.102	-0.106
DAN/DRA	0.469	0.119	0.151	0.185	0.300
DAN/DRP	0.545	0.097	0.125	0.157	0.263
DAN/DCMOM	-1.621	-2.148	-1.878	-1.961	-1.911
TMIN,TMAX	0.0018 0.0625	0.0015 0.1592	0.0015 0.2025	0.0016 0.2500	0.0016 0.3600

TABLE IX

RESULTS FOR K^-p SCATTERING

MOMENTUM	70	125	150	175	200
RHO	0.171±0.040	0.122±0.029	0.123±0.031	0.125±0.029	0.161±0.032
RSTAT,RSYS	0.039 0.012	0.027 0.009	0.030 0.008	0.027 0.010	0.029 0.014
U	1.400 --	1.610±0.170	1.909±0.153	2.095±0.126	1.959±0.084
USTAT,USYS	-- --	0.170 0.007	0.153 0.004	0.126 0.006	0.084 0.006
AM	0.863±0.027	1.026±0.022	1.013±0.023	1.008±0.020	1.054±0.021
SIGT	20.380	20.590	20.600	20.670	20.760
CHI/D.F.	1.016	1.043	1.079	1.349	1.147
D.F.	104	120	137	92	112
EVENTS (K)	23	97	73	75	95
MPTYERR	0.064	0.041	0.052	0.024	0.028
DR/DU	-0.064	-0.128	-0.142	-0.153	-0.221
DR/DAM	-1.372	-1.176	-1.256	-1.269	-1.309
DR/DMPTY	-0.072	-0.075	-0.119	-0.085	-0.332
DR/DSIGT	0.079	0.078	0.074	0.073	0.069
DR/DRA	-0.524	-0.061	-0.091	-0.106	-0.205
DR/DRP	-0.808	-0.118	-0.159	-0.199	-0.372
DR/DCMON	2.986	2.906	2.906	2.929	2.839
DU/DAM	--	7.058	6.156	5.614	3.455
DU/DMPTY	--	-0.150	0.008	-0.042	0.111
DU/DSIGT	--	-0.070	-0.078	-0.064	-0.041
DU/DRA	--	-7.392	-7.141	-6.989	-6.494
DU/DRP	--	-11.176	-10.769	-10.452	-9.582
DU/DCMON	--	-0.741	-2.182	-1.762	-1.321
DAM/DMPTY	0.011	0.001	0.026	0.013	0.131
DAM/DSIGT	-0.114	-0.133	-0.131	-0.129	-0.135
DAM/DRA	0.463	0.074	0.098	0.112	0.207
DAM/DRP	0.717	0.137	0.172	0.207	0.372
DAM/DCMON	-1.941	-2.252	-2.331	-2.317	-2.488
TMIN,TMAX	0.0018 0.0625	0.0015 0.1592	0.0015 0.2025	0.0016 0.2500	0.0016 0.3600

TABLE X

Results of Fitting the pp Cross Sections of Jenkins et al.

with the Form Factor Formulation[a]

Momentum (GeV/c)	ρ_J	ρ_{ff}	u^b $(GeV/c)^{-2}$	σ_{tot}^c (mb)	Λ_n	χ^2/DF	$-t_{min}$ $(GeV/c)^2$	$-t_{max}$ $(GeV/c)^2$
50	-0.153 ± 0.012	-0.140 ± 0.013	0.08	38.33	1.01 ± 0.01	1.36	0.0016	0.0309
80	-0.096 ± 0.010	-0.075 ± 0.011	0.64	38.33	1.02 ± 0.01	0.97	0.0007	0.0293
199	-0.034 ± 0.009	0.023 ± 0.008	1.79	38.99	1.03 ± 0.01	1.11	0.0007	0.0315
261	-0.009 ± 0.009	0.026 ± 0.009	2.13	39.33	1.01 ± 0.02	0.96	0.0005	0.0298
303	-0.011 ± 0.008	0.028 ± 0.008	2.32	39.59	1.04 ± 0.01	1.26	0.0007	0.0316
398	0.012 ± 0.009	0.052 ± 0.008	2.66	40.80	1.04 ± 0.01	1.17	0.0005	0.0258

[a]The quantities ρ_J are from Jenkins et al., while ρ_{ff} are from these fits.

[b]The values of u were obtained from an a + b ln(momentum) fit to our values of u.

[c]The total cross sections used are those used by Jenkins et al.

FIGURE CAPTIONS

FIG. 1 Plan view of experimental apparatus (not to scale left of vertical dashed line).

FIG. 2 Veto plane geometry. The small rectangle represents the counter V; the shaded region denotes the projection of the downstream spectrometer magnet onto the veto plane; and the X indicates where the beam axis enters the page. The circles are the loci of particles with 200 GeV/c incident momentum that scattered from the beam axis with the indicated values of $|t|$ in units of $(GeV/c)^2$.

FIG. 3 Schematic representation of HFSD calculations.

FIG. 4 HSD efficiency in the x direction as a function of q_x at (a) 70 GeV/c and (b) 200 GeV/c. The error bars indicate the statistical uncertainty of the curves.

FIG. 5 Apparatus resolution as a function of momentum: (a) q resolution and (b) recoil mass squared. The solid line is the constant contribution due to multiple scattering, while the vertically striped band is the angle dependent PWC resolution. The horizontally striped band is the sum in quadrature of these two contributions.

FIG. 6 Apparatus acceptance as a function of q at 200 GeV/c.

FIG. 7 $d\sigma/dt$ versus t for pp elastic scattering at 200 GeV/c. The theoretical curve is the exponential cross section with C = 0 fit to the data in the range $0.0016 \leq -t \leq 0.09\ (GeV/c)^2$.

FIG. 8 Local slopes as a function of t for pp, π^+p, and π^-p elastic scattering. The solid line is the form factor slope, $b^{ff}(t)$, as determined from the values of u in Tables IV, V, and VII and is extended beyond the t range of the fits by the dotted line. The dashed line represents the envelope of the uncertainties of the local slopes from fits made to our data using the same t intervals employed by Schiz et al.

FIG. 9 Local slopes as a function of momentum at $-t = 0.1$ and 0.2 $(GeV/c)^2$ for (a) pp, (b) π^+p, (c) K^+p, (d) $\bar{p}p$, (e) π^-p, and K^-p elastic scattering. The slopes from this experiment are calculated using $b^{ff}(t)$ with the values of u from Tables IV - IX. The slopes of Ayres et al. and Akerlof et al. are calculated using $b^e(t)$ with their values of B and C.

FIG. 10 Sensitivity of the parameters to the upper limit of the t range of the fit at 200 GeV/c for pp, π^+p, K^+p, $\bar{p}p$, π^-p, and K^-p. The form factor cross section and the exponential cross section with $C = 0$ were fit to the data over the t range $0.0016\ (GeV/c)^2 \leq -t \leq -t_{max}$. In (a) the resulting slope parameters, u and B are arbitrarily superimposed. In (b) the resulting values of ρ are shown. For both (a) and (b) the dashed line is drawn through the values found in Tables IV - IX.

FIG. 11 $d\sigma/dt$ versus $-t$ at all incident momenta for (a) pp, (b) π^+p, (c) K^+p, (d) $\bar{p}p$, (e) π^-p, and (f) K^-p elastic scattering. The cross sections have been multiplied by the indicated factor.

FIG. 12 $d\sigma/dt$ measured and $d\sigma/dt$ theoretical (solid line) divided by $d\sigma/dt$ theoretical but with $\rho = 0$ for (a) pp, (b) π^+p, (c) K^+p, (d) $\bar{p}p$, (e) π^-p, and (f) K^-p. $d\sigma/dt$ theoretical is the form factor cross section as parametrized in Tables IV - IX. The dashed line is to guide the eye.

FIG. 13 ρ as a function of momentum for (a) pp, (b) π^+p, (c) K^+p, (d) $\bar{p}p$, (e) π^-p, and (f) K^-p. The curves are dispersion relation predictions.

FIG. 14 ρ for pp elastic scattering versus momentum but with Jenkins et al.'s data refitted (See text and Table X).

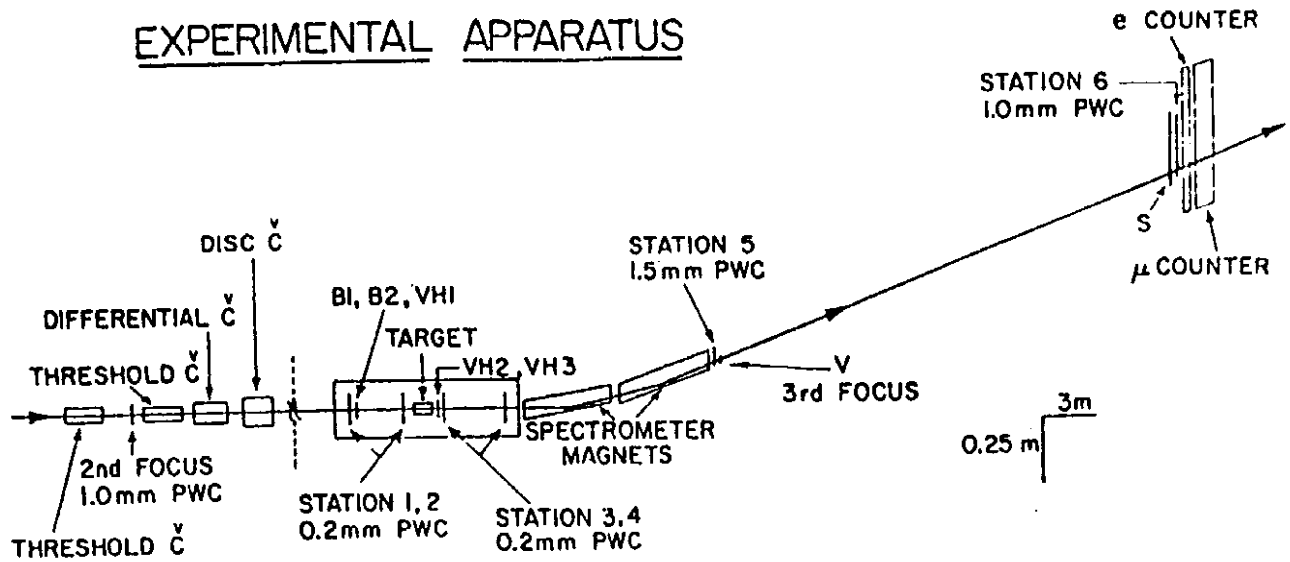
EXPERIMENTAL APPARATUS
DISC Č
DIFFERENTIAL Č
THRESHOLD Č
2nd FOCUS
1.0mm PWC
THRESHOLD Č
B1, B2, VH1
TARGET
VH2, VH3
STATION 1, 2
0.2mm PWC
STATION 3, 4
0.2mm PWC
SPECTROMETER
MAGNETS
STATION 5
1.5mm PWC
V
3rd FOCUS
STATION 6
1.0mm PWC
e COUNTER
S
μ COUNTER
3m
0.25 m

Figure 1

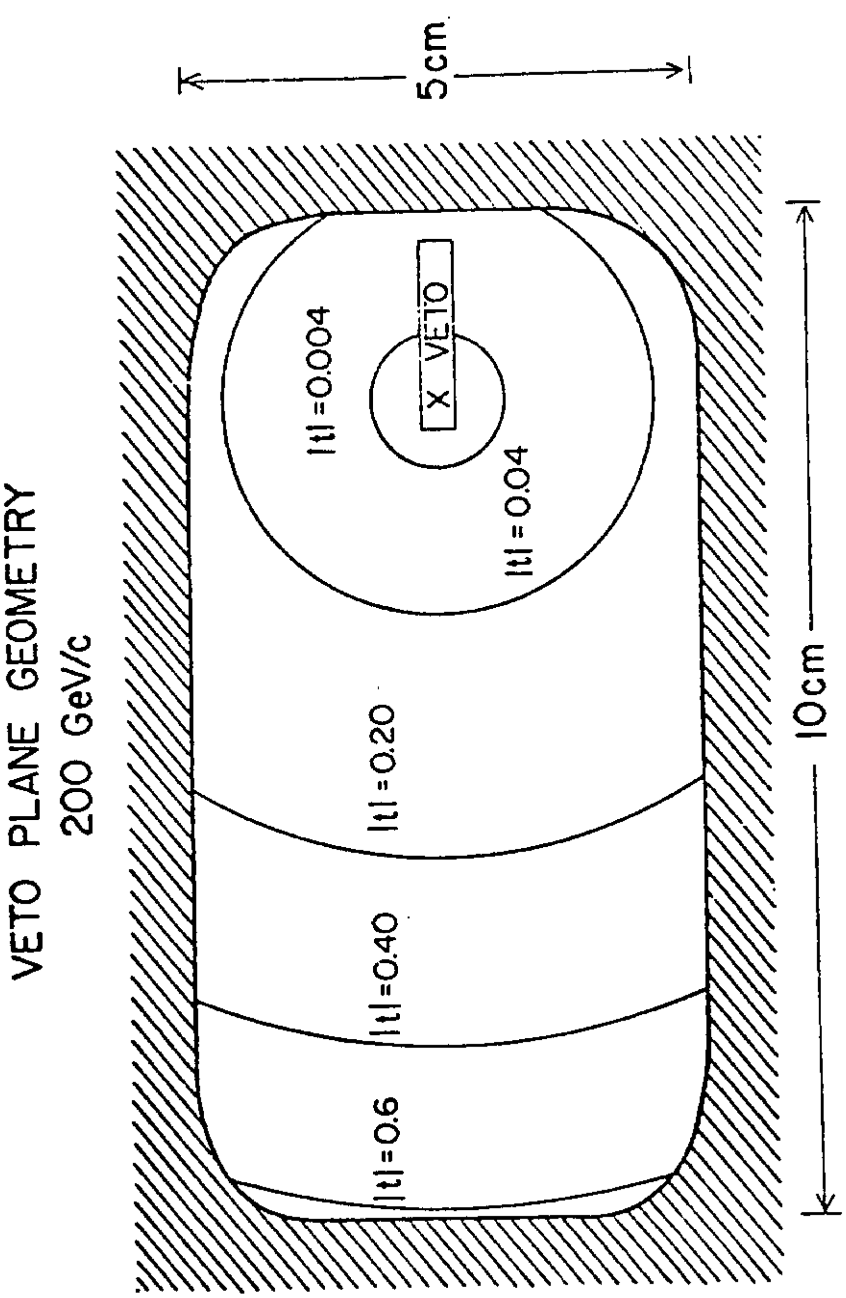
VETO PLANE GEOMETRY
200 GeV/c
5cm
10cm
|t|=0.004
X VETO
|t|=0.04
|t|=0.20
|t|=0.40
|t|=0.6

Figure 2

HFD and HSD Geometry

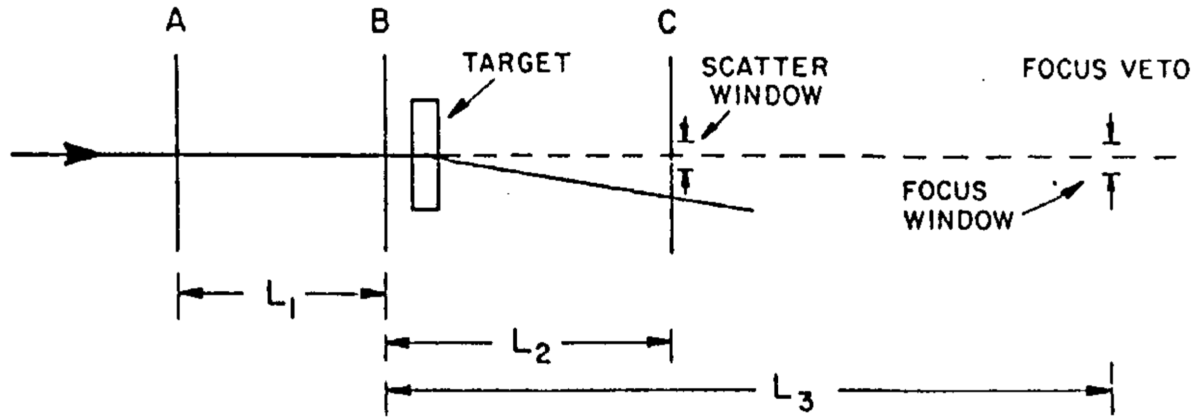

SCATTER: $\frac{L_2}{L_1} A + C - \left(\frac{L_1 + L_2}{L_1} \right) B >$ Scatter Window

FOCUS: $\frac{L_3}{L_1} A - \left(1 + \frac{L_3}{L_1} \right) B <$ Focus Window

Figure 3

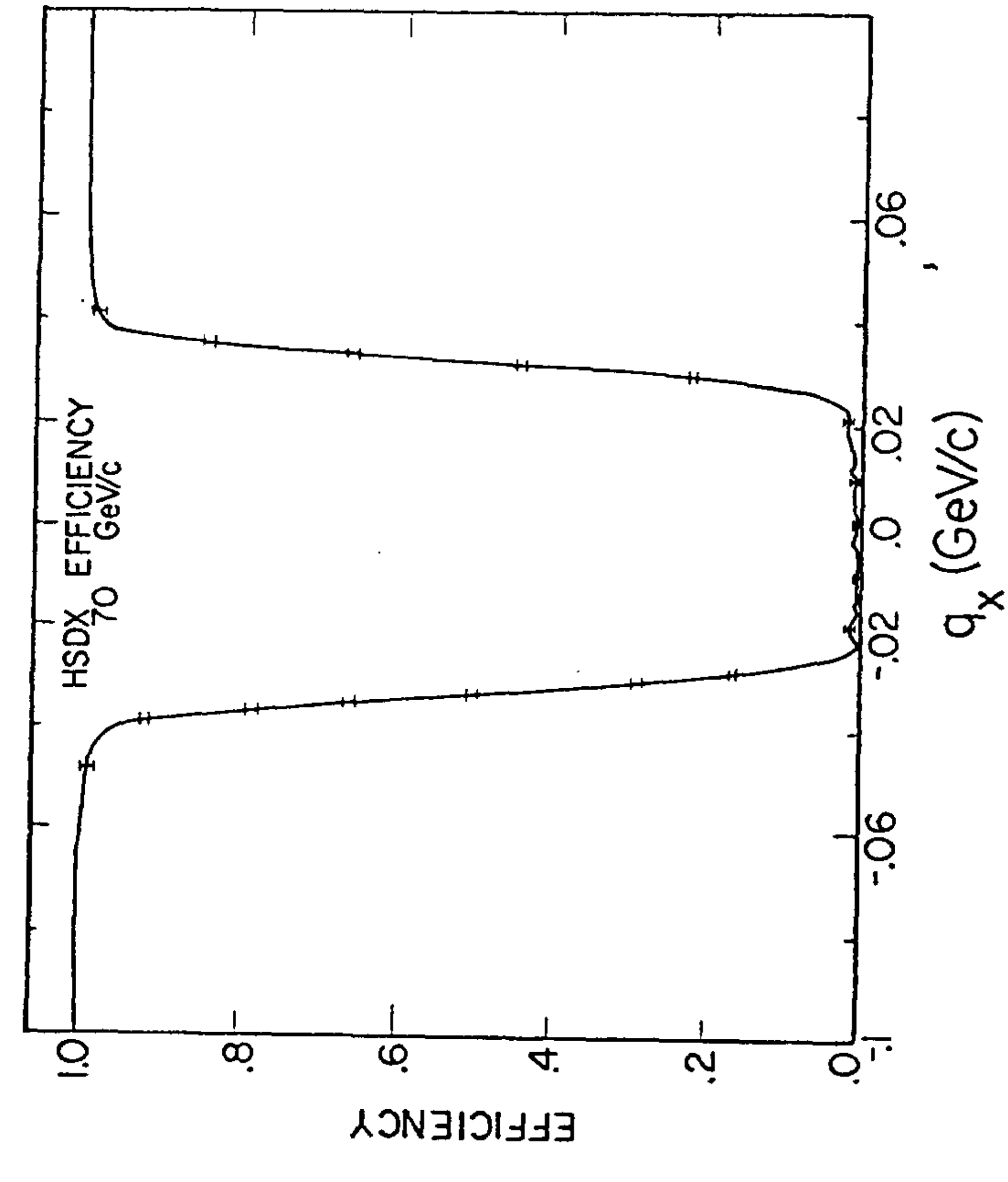
HSDX 70 GeV/c EFFICIENCY
EFFICIENCY
1.0
.8
.6
.4
.2
0
-.1
-.06
-.02
0
.02
.06
.1
q_x (GeV/c)

Figure 4a

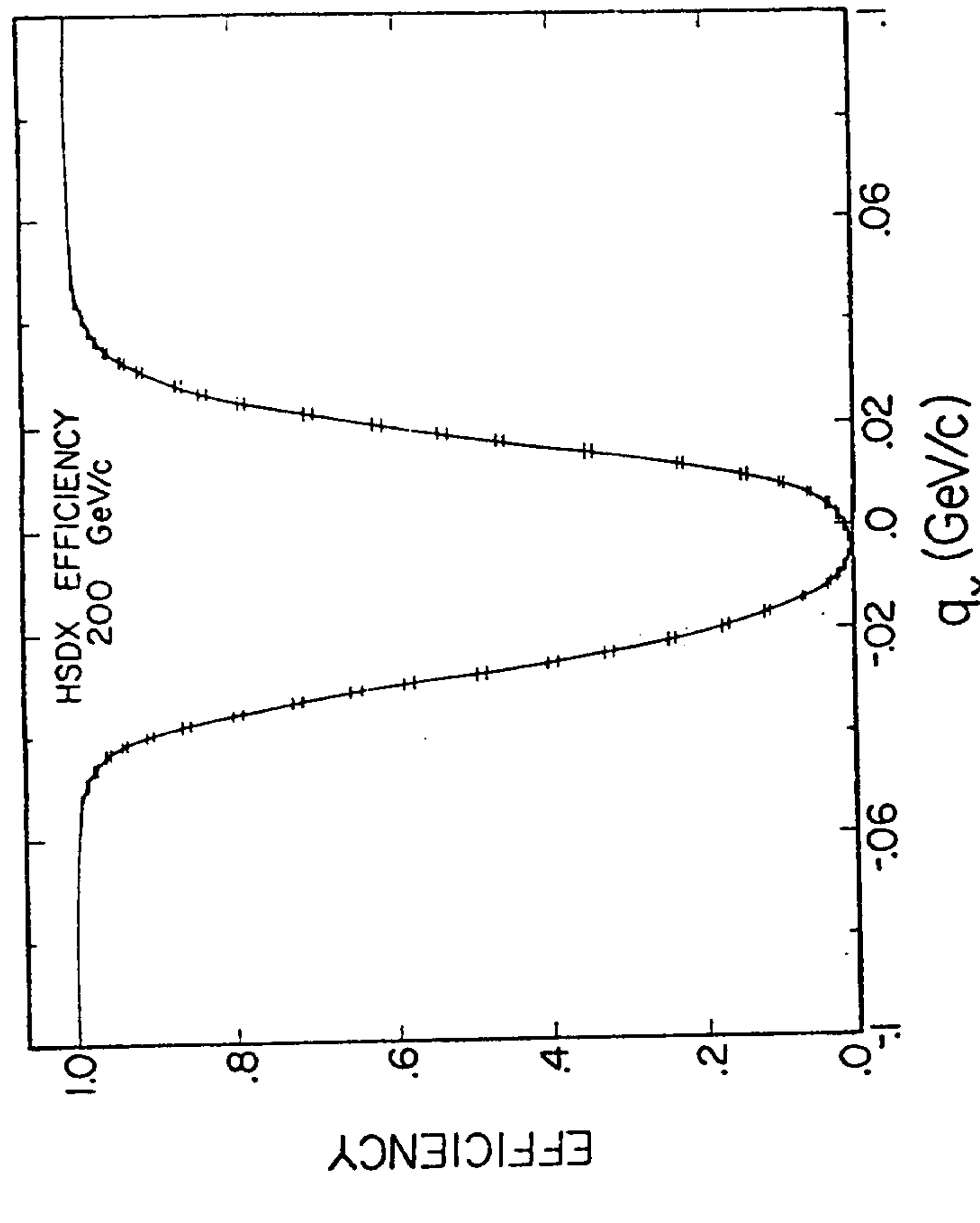
HSDX EFFICIENCY
200 GeV/c
EFFICIENCY
1.0
.8
.6
.4
.2
0.
-.1
-.06
-.02
.0
.02
.06
.1
q_x (GeV/c)

Figure 4b

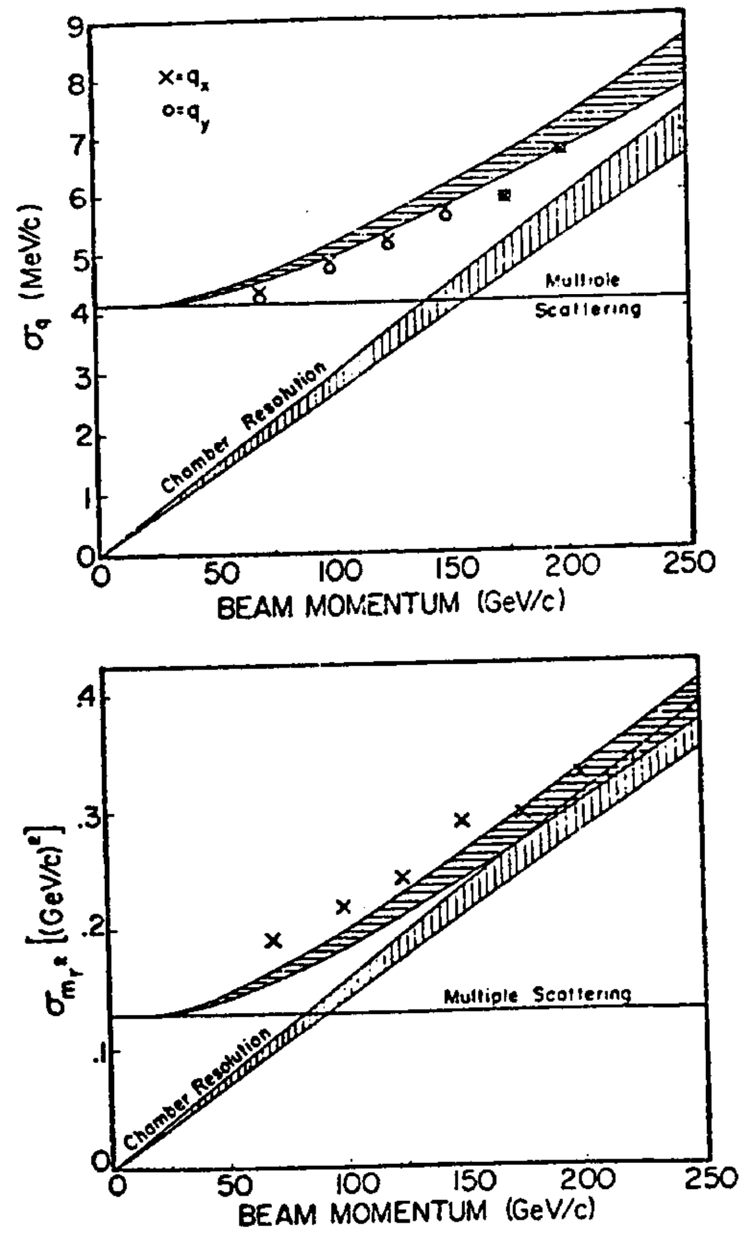
×=q_x
o=q_y
σ_q (MeV/c)
Multiple Scattering
Chamber Resolution
BEAM MOMENTUM (GeV/c)
$\sigma_{m_r^2}$ [(GeV/c)^2]
Multiple Scattering
Chamber Resolution
BEAM MOMENTUM (GeV/c)

Figure 5

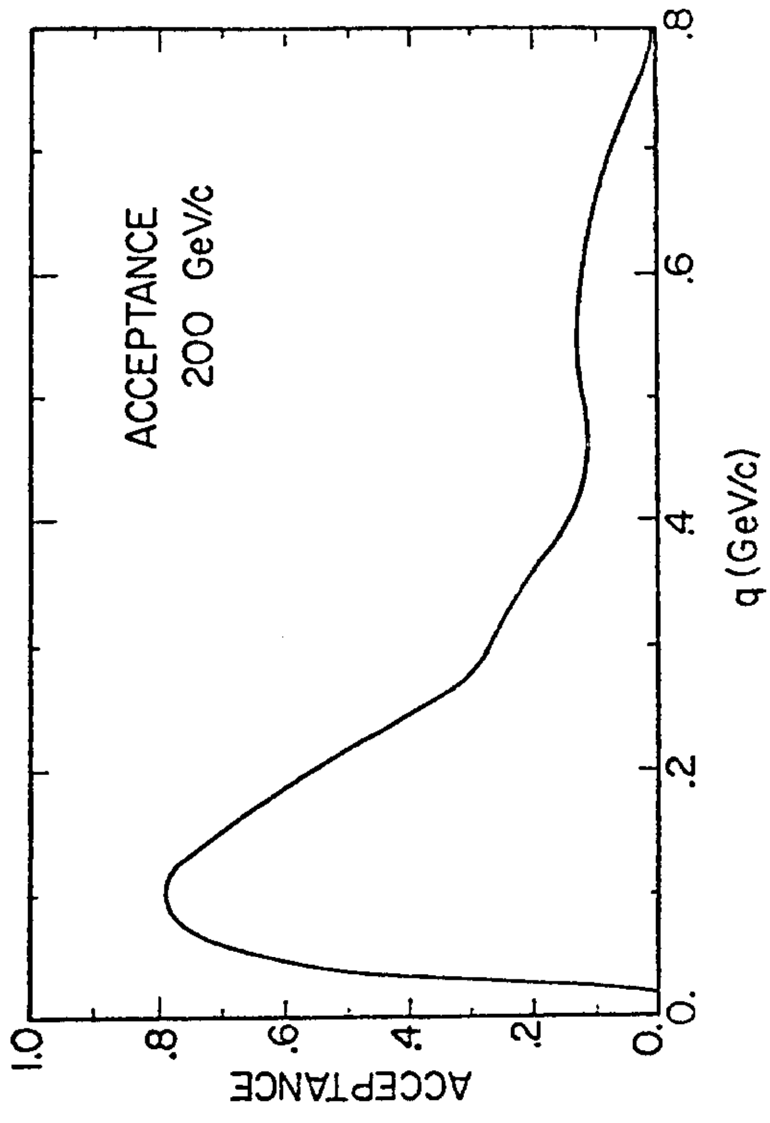

Figure 6

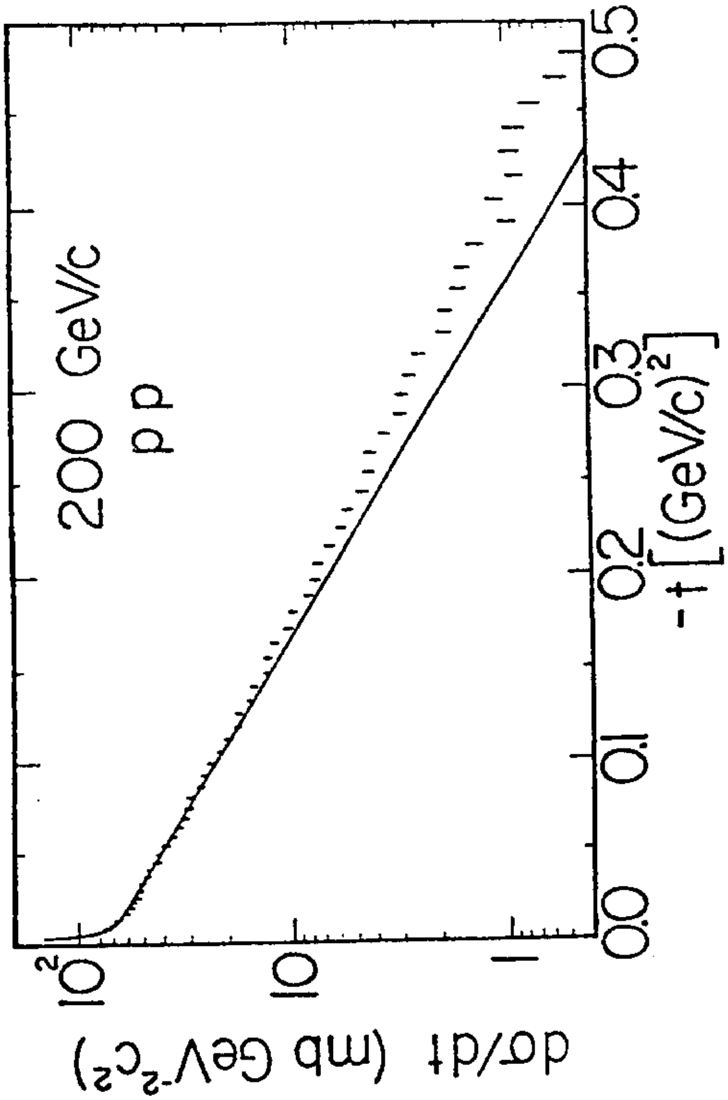

Fig. 7

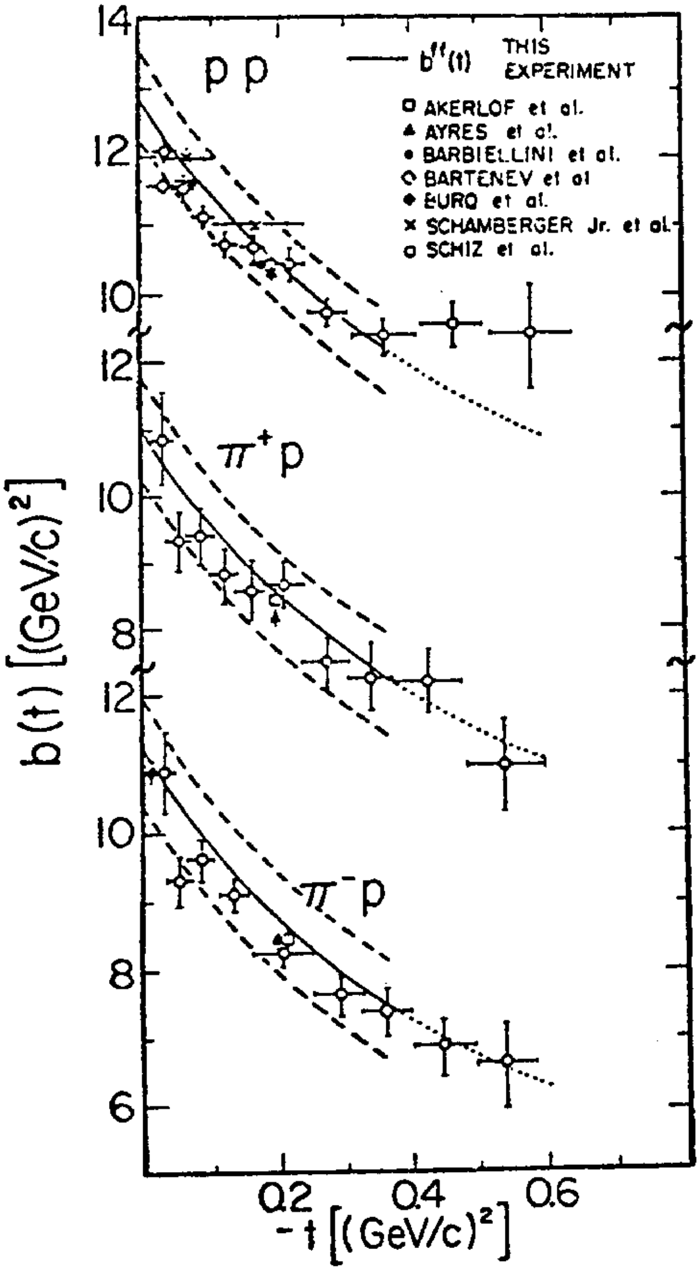

14
12
10
12
10
8
12
10
8
6
p p
$\pi^+ p$
$\pi^- p$
b(t) [(GeV/c)²]
— $b^{ff}(t)$ THIS EXPERIMENT
AKERLOF et al.
AYRES et al.
BARBIELLINI et al.
BARTENEV et al
EURO et al.
SCHAMBERGER Jr. et al.
SCHIZ et al.
0.2
0.4
0.6
-t [(GeV/c)²]

Figure 8

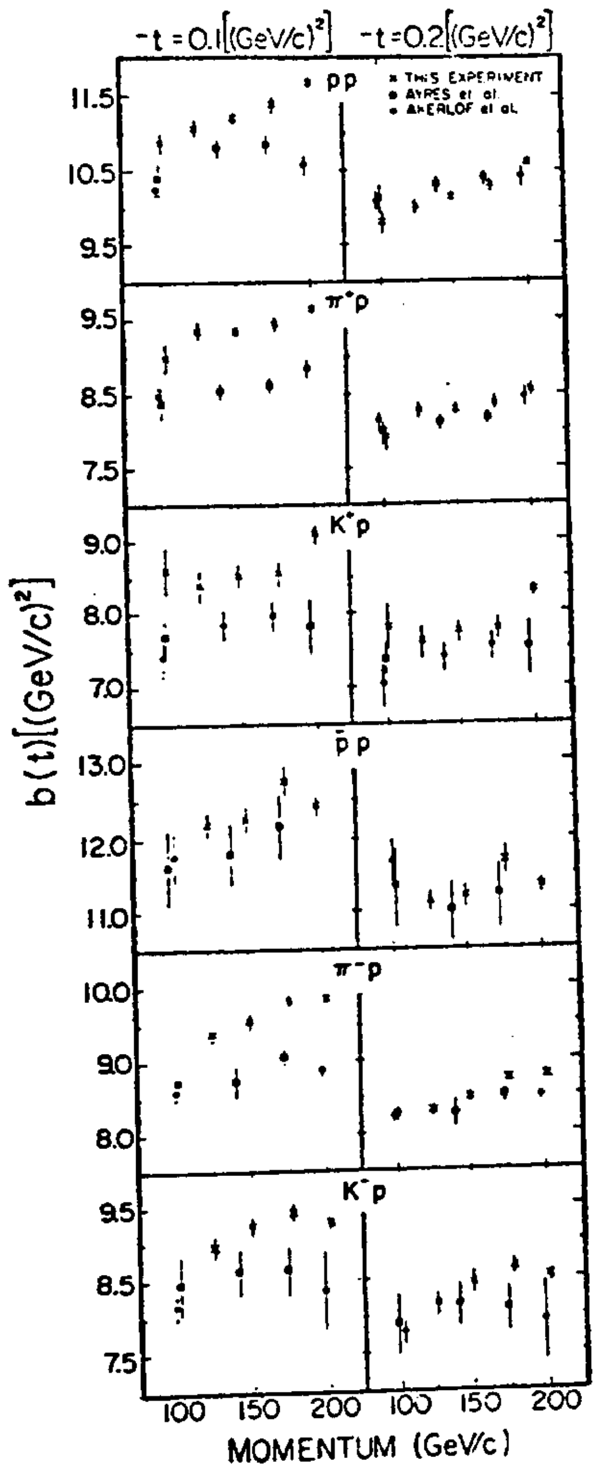
-t = 0.1 [(GeV/c)²]
-t = 0.2 [(GeV/c)²]
pp
THIS EXPERIMENT
AYRES et al.
AKERLOF et al.
π⁺p
K⁺p
p̄p
π⁻p
K⁻p
b(t) [(GeV/c)²]
MOMENTUM (GeV/c)

Figure 9

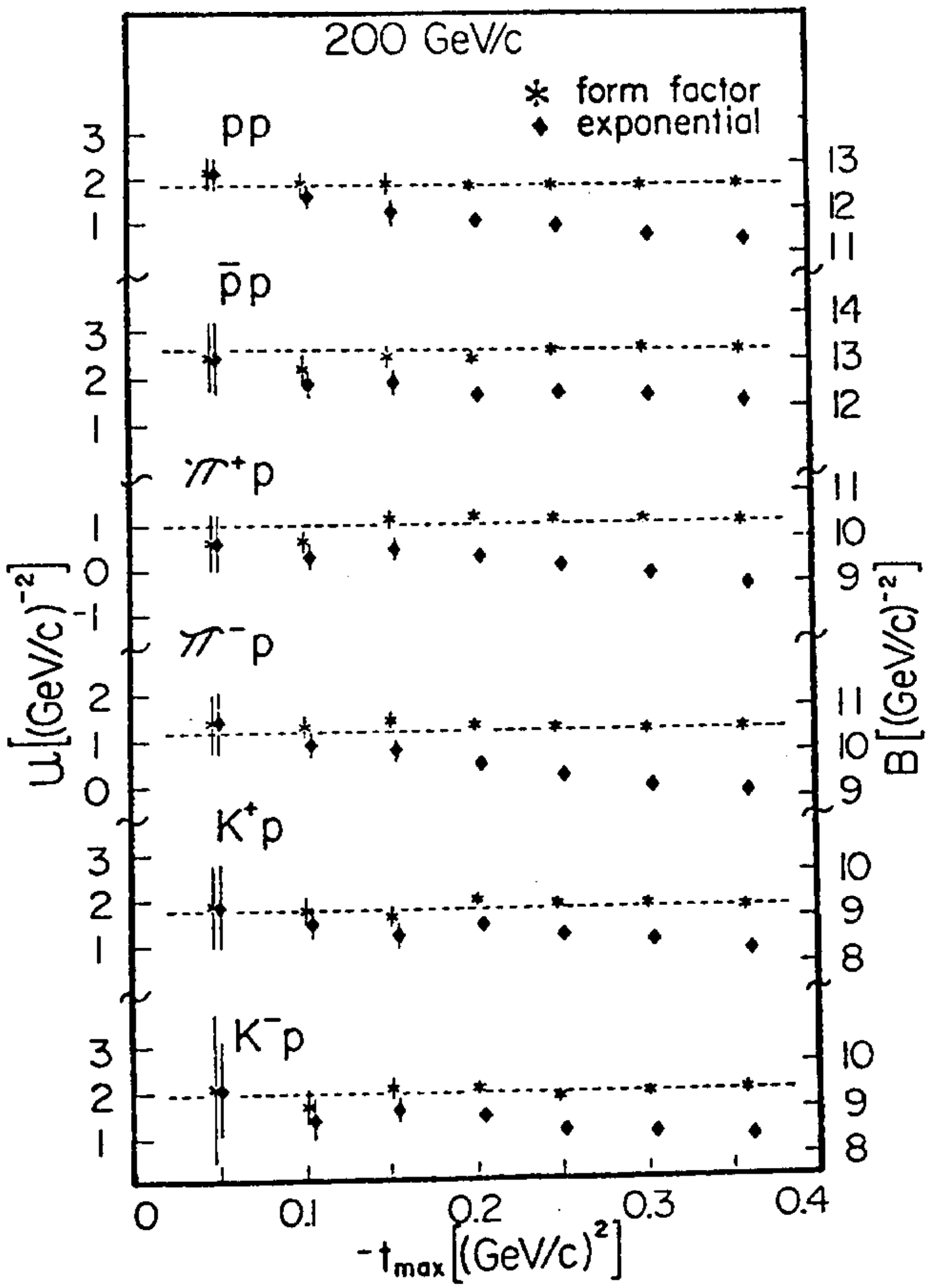
200 GeV/c
form factor
exponential
pp
p̄p
π⁺p
π⁻p
K⁺p
K⁻p
u[(GeV/c)⁻²]
B[(GeV/c)⁻²]
-t_max[(GeV/c)²]
0
0.1
0.2
0.3
0.4

Figure 10a

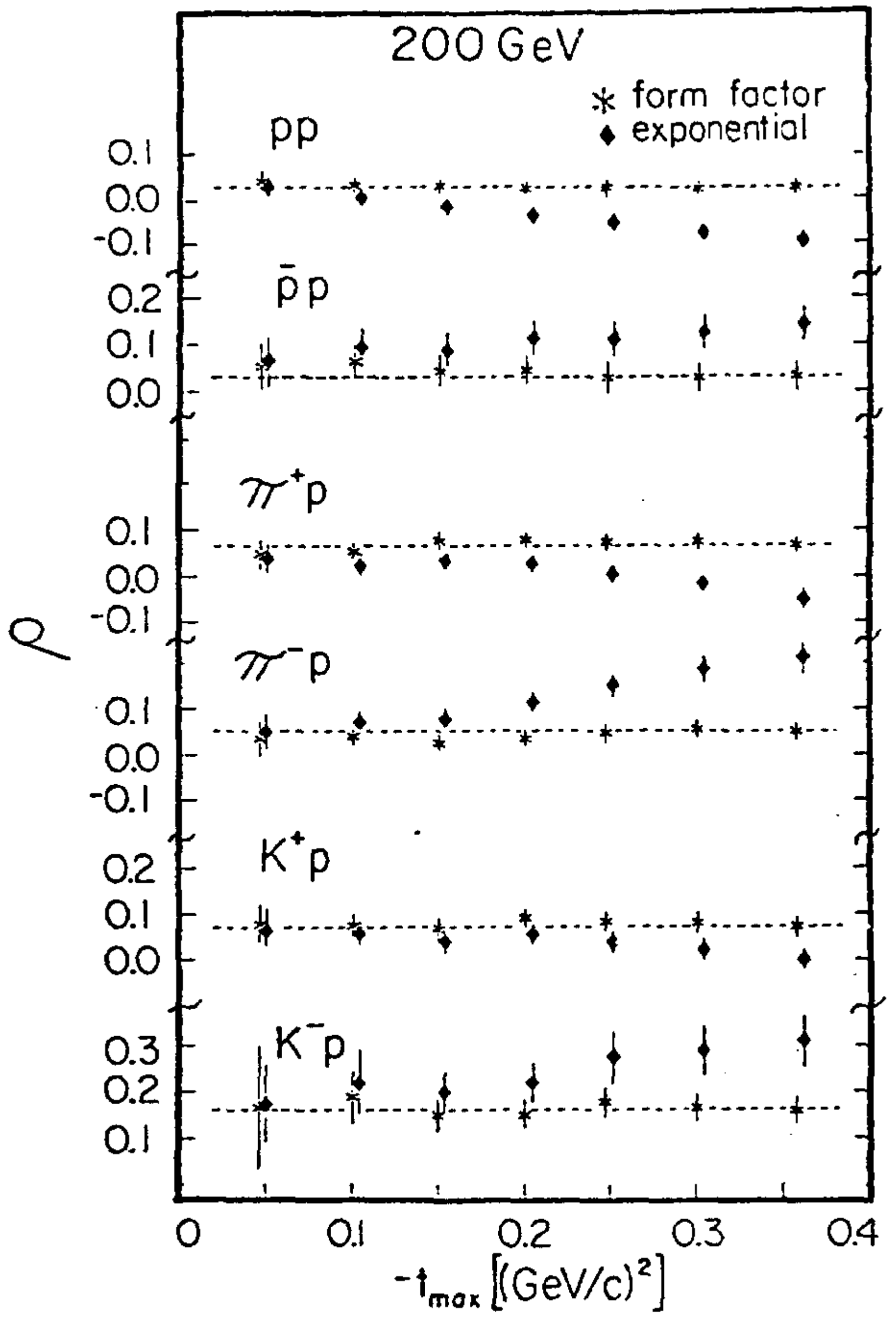
200 GeV
⁎ form factor
♦ exponential
pp
$\bar{p}p$
π^+p
π^-p
K^+p
K^-p
ρ
0.1
0.0
-0.1
0.2
0.3
0
0.1
0.2
0.3
0.4
$-t_{max}$ [(GeV/c)^2]

Figure 10b

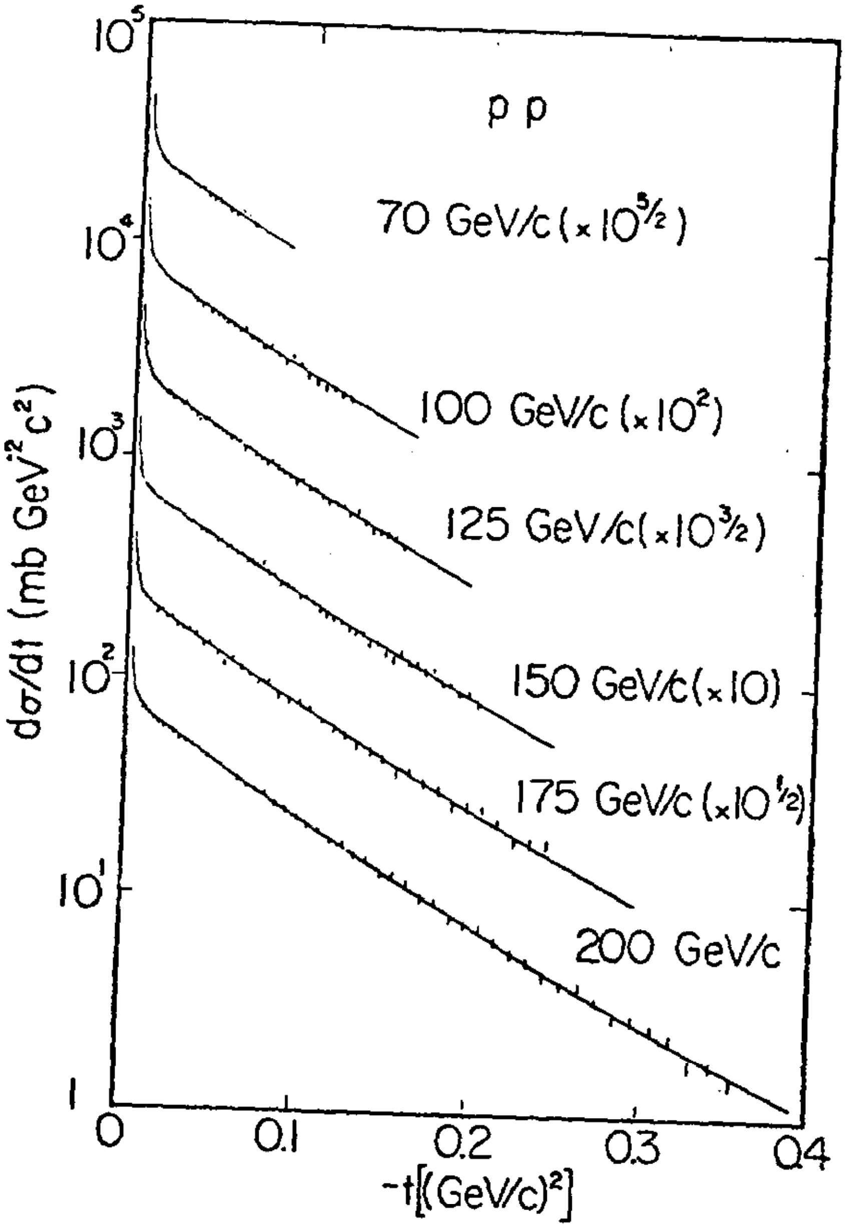
p p
70 GeV/c (×10^5/2)
100 GeV/c (×10^2)
125 GeV/c (×10^3/2)
150 GeV/c (×10)
175 GeV/c (×10^1/2)
200 GeV/c
dσ/dt (mb GeV^-2 c^2)
-t [(GeV/c)^2]
10^5
10^4
10^3
10^2
10^1
1
0
0.1
0.2
0.3
0.4

Figure 11a

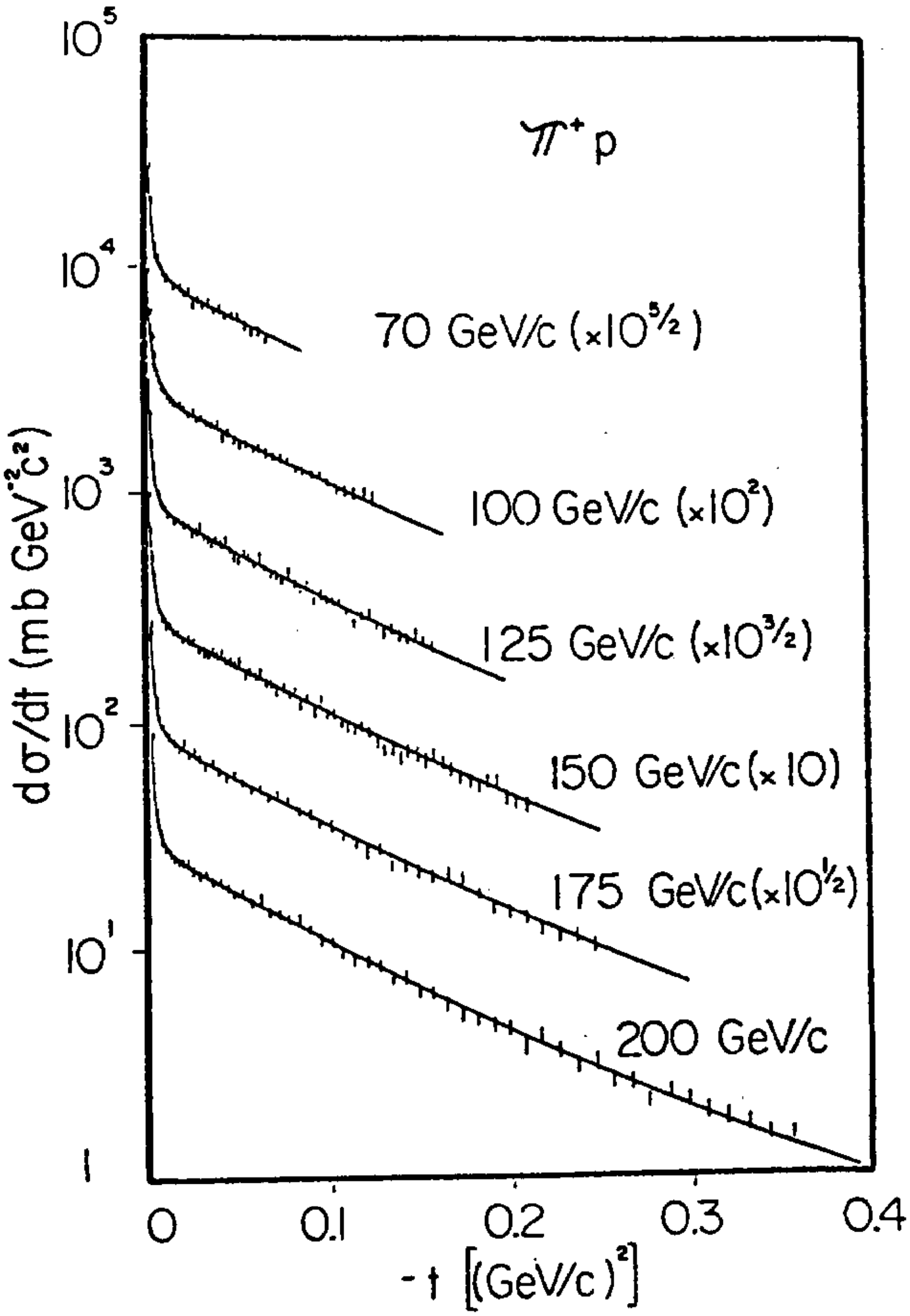
$\pi^+ p$
70 GeV/c ($\times 10^{5/2}$)
100 GeV/c ($\times 10^2$)
125 GeV/c ($\times 10^{3/2}$)
150 GeV/c ($\times 10$)
175 GeV/c ($\times 10^{1/2}$)
200 GeV/c
$d\sigma/dt$ (mb GeV^{-2}c^2)
$-t$ [(GeV/c)^2]
10^5
10^4
10^3
10^2
10^1
1
0
0.1
0.2
0.3
0.4

Figure 11b

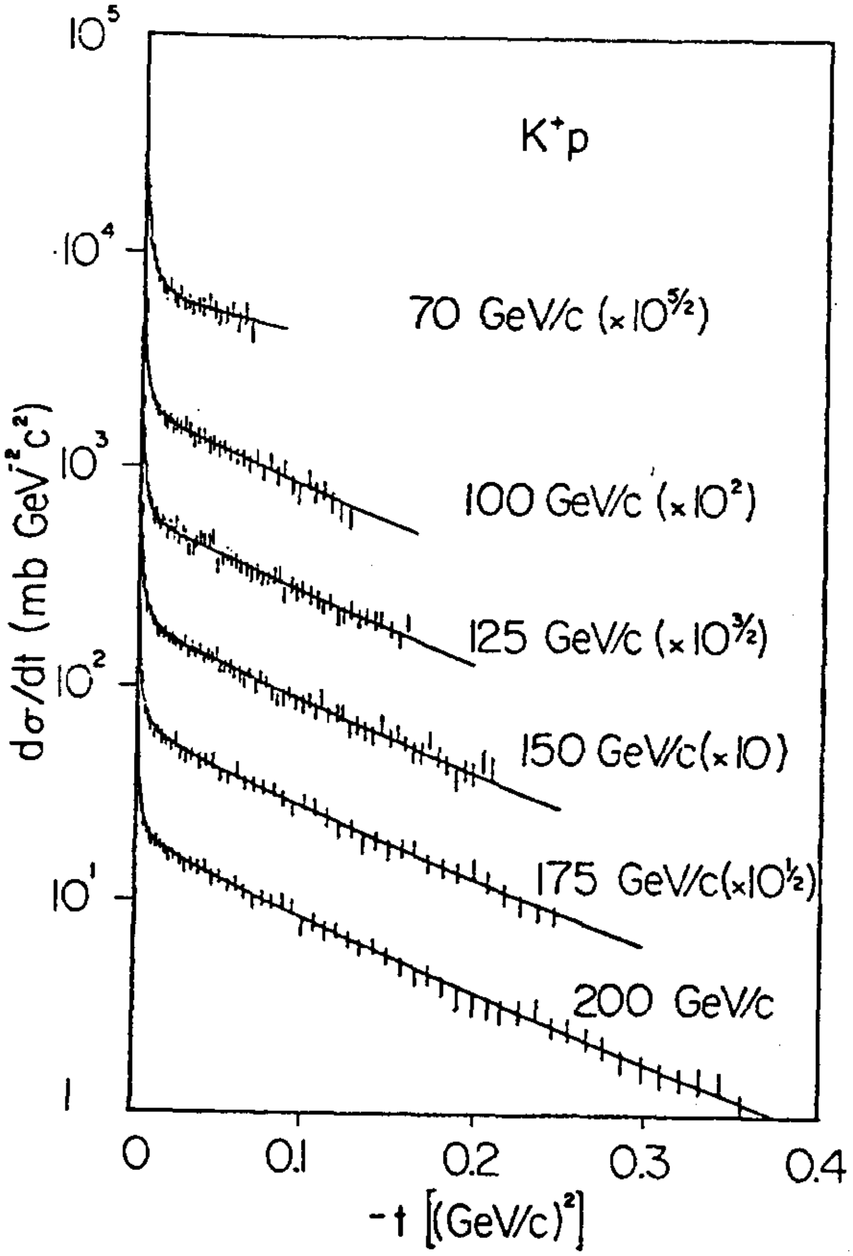
K⁺p
70 GeV/c (×10^5/2)
100 GeV/c (×10²)
125 GeV/c (×10^3/2)
150 GeV/c(×10)
175 GeV/c(×10^1/2)
200 GeV/c
dσ/dt (mb GeV⁻²c²)
-t [(GeV/c)²]
10⁵
10⁴
10³
10²
10¹
1
0
0.1
0.2
0.3
0.4

Figure 11c

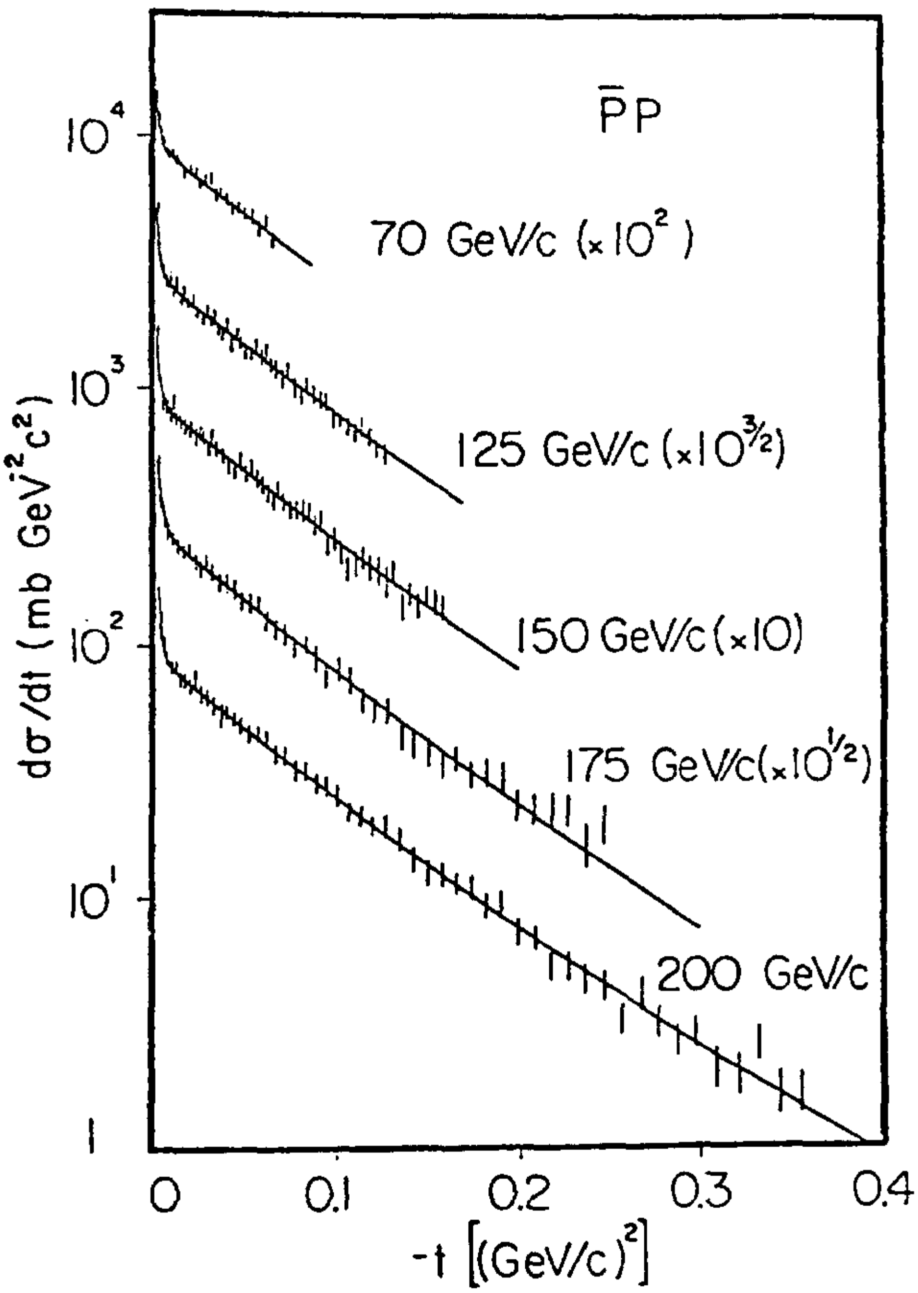
P̄P
70 GeV/c (×10²)
125 GeV/c (×10^3/2)
150 GeV/c (×10)
175 GeV/c (×10^1/2)
200 GeV/c
10⁴
10³
10²
10¹
1
dσ/dt (mb GeV⁻²c²)
0
0.1
0.2
0.3
0.4
-t [(GeV/c)²]

Figure 11d

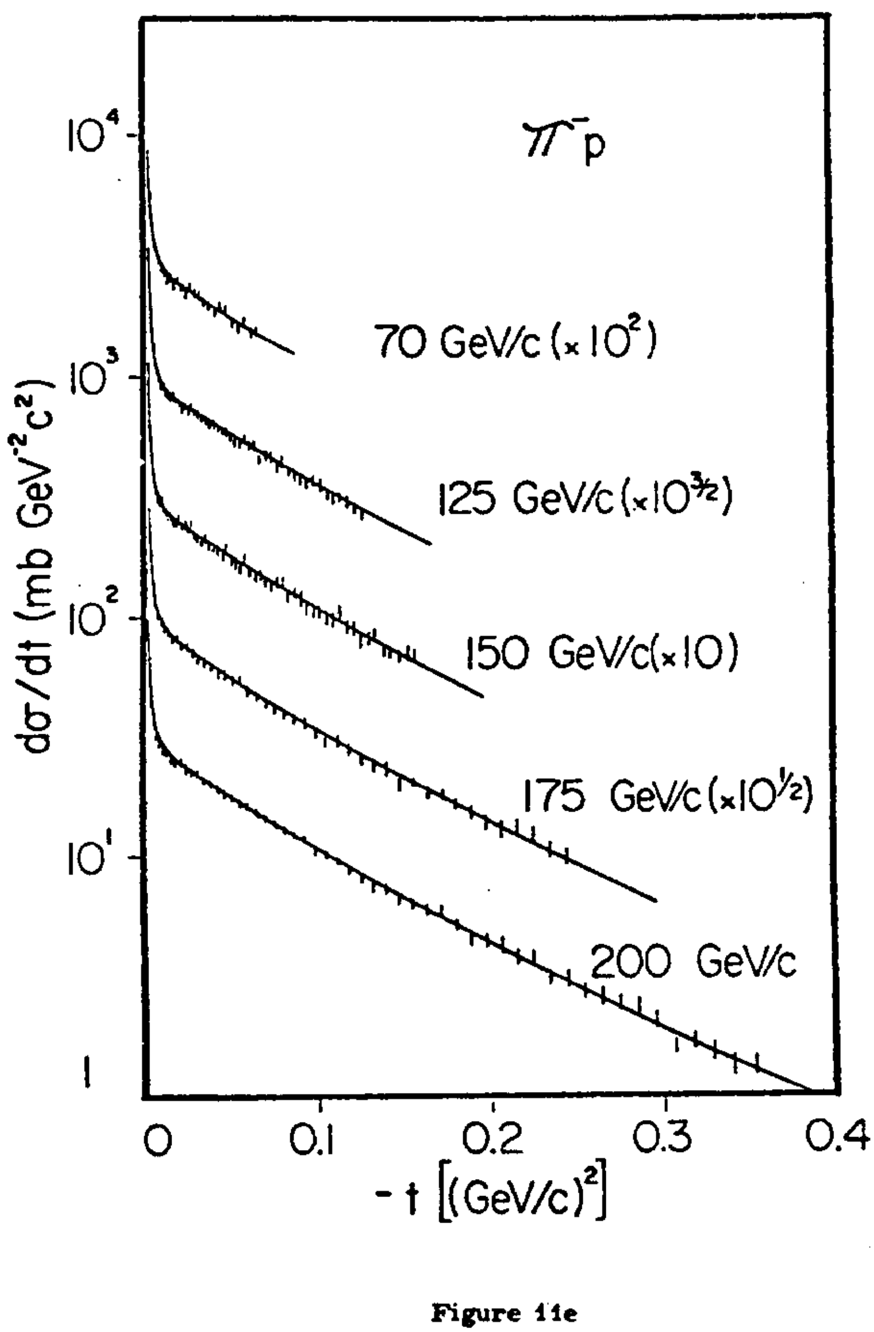

$\pi^- p$
70 GeV/c (×10²)
125 GeV/c (×10^{3/2})
150 GeV/c(×10)
175 GeV/c (×10^{1/2})
200 GeV/c
dσ/dt (mb GeV⁻²c²)
10⁴
10³
10²
10¹
1
0
0.1
0.2
0.3
0.4
- t [(GeV/c)²]

Figure 11e

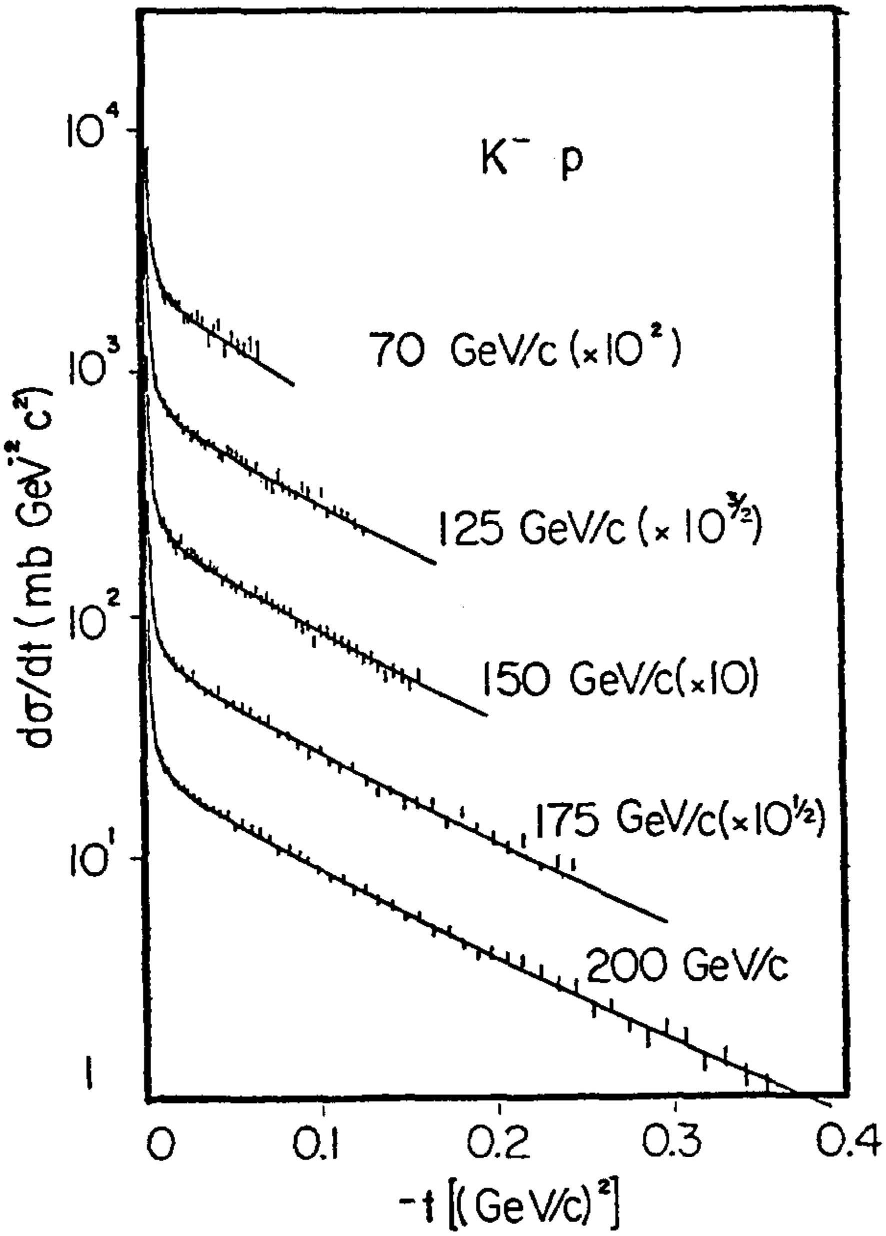
K⁻ p
70 GeV/c (×10²)
125 GeV/c (× 10^{3/2})
150 GeV/c(×10)
175 GeV/c(×10^{1/2})
200 GeV/c
dσ/dt (mb GeV⁻² c²)
10⁴
10³
10²
10¹
1
0
0.1
0.2
0.3
0.4
-t [(GeV/c)²]

Figure 11f

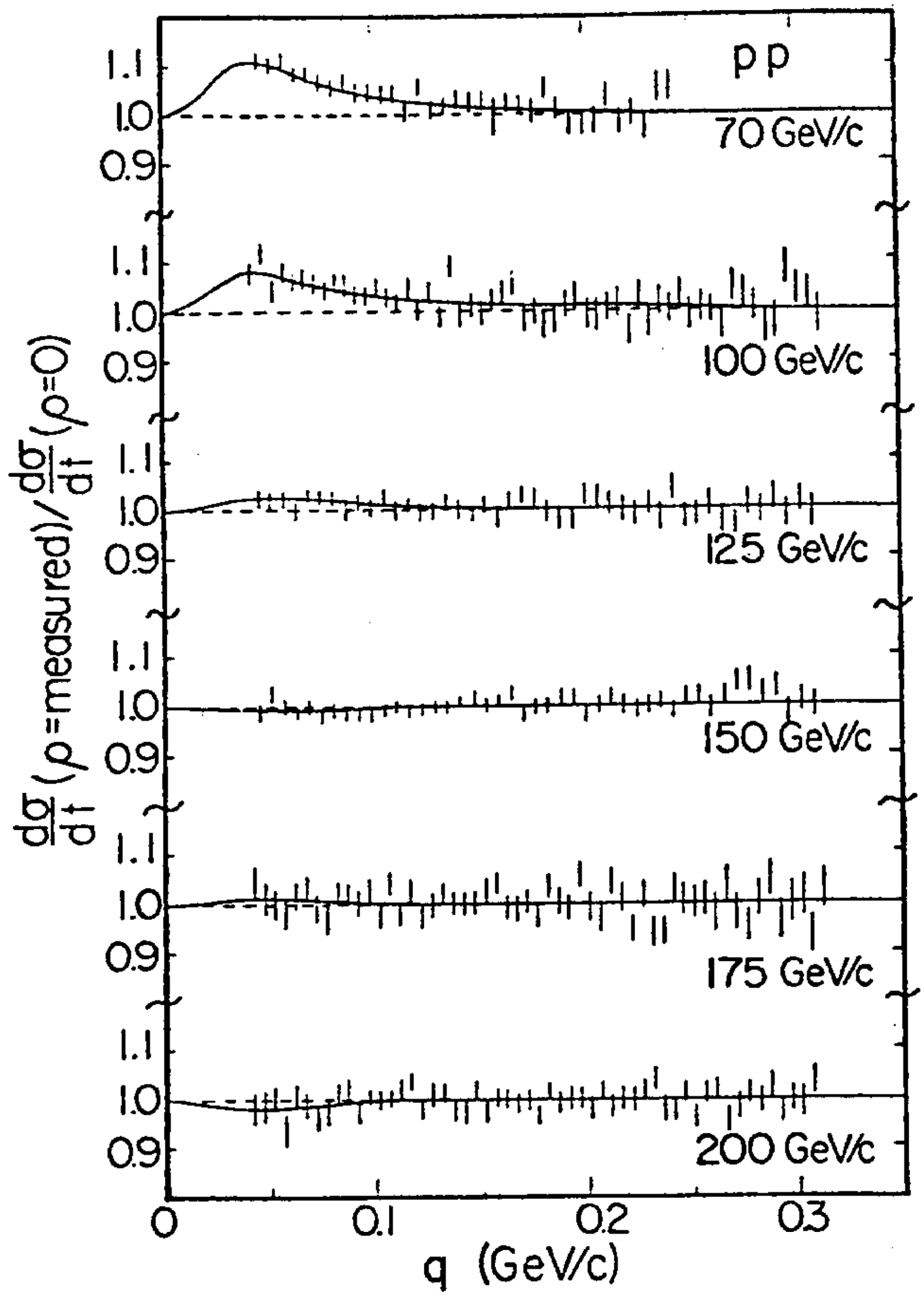
pp
1.1
1.0
0.9
70 GeV/c
100 GeV/c
125 GeV/c
150 GeV/c
175 GeV/c
200 GeV/c
0
0.1
0.2
0.3
q (GeV/c)
dσ/dt (ρ=measured)/ dσ/dt (ρ=0)

Figure 12a

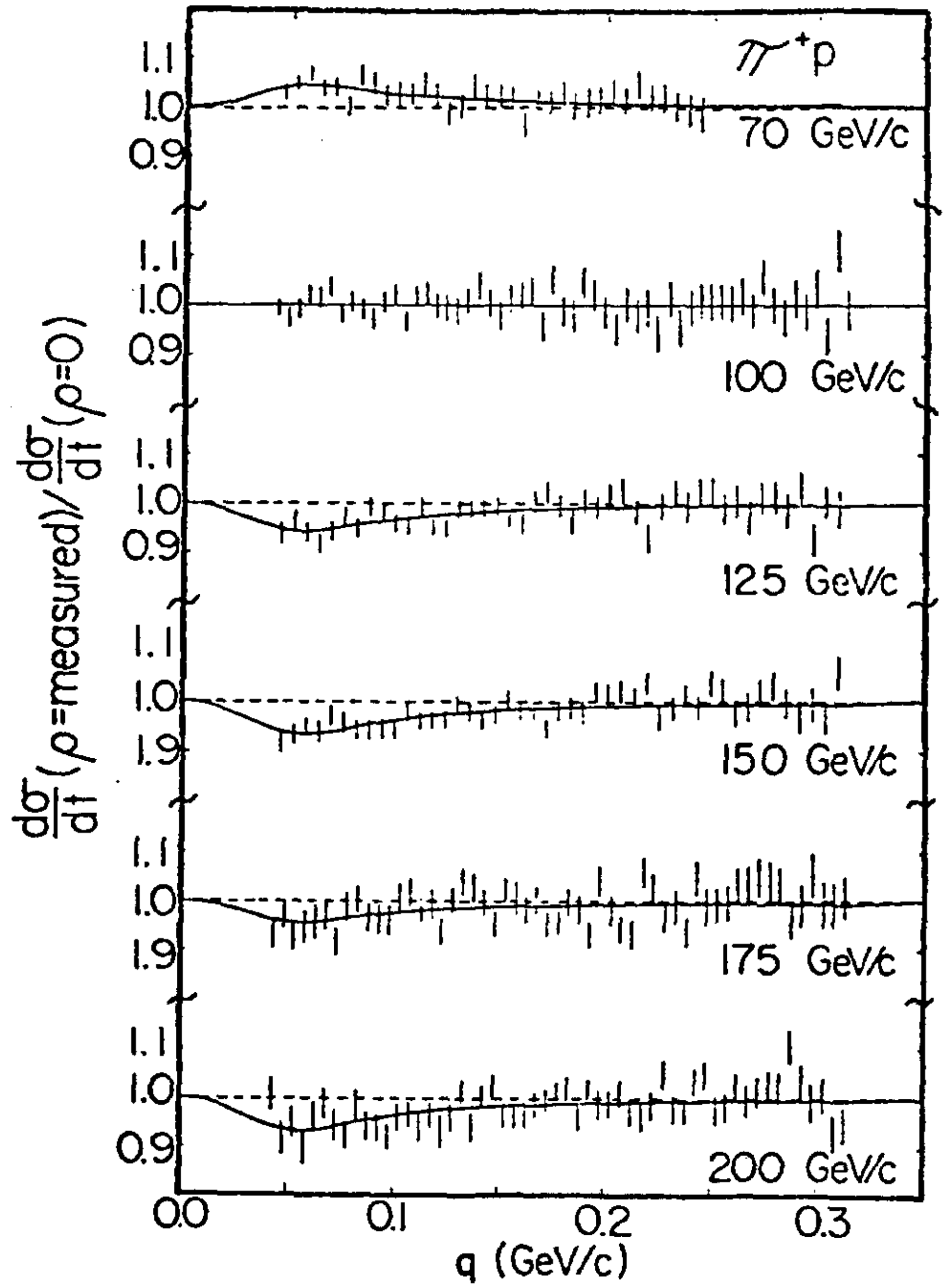
π^+p
70 GeV/c
100 GeV/c
125 GeV/c
150 GeV/c
175 GeV/c
200 GeV/c
1.1
1.0
0.9
$\frac{d\sigma}{dt}(\rho=\text{measured})/\frac{d\sigma}{dt}(\rho=0)$
0.0
0.1
0.2
0.3
q (GeV/c)

Figure 12b

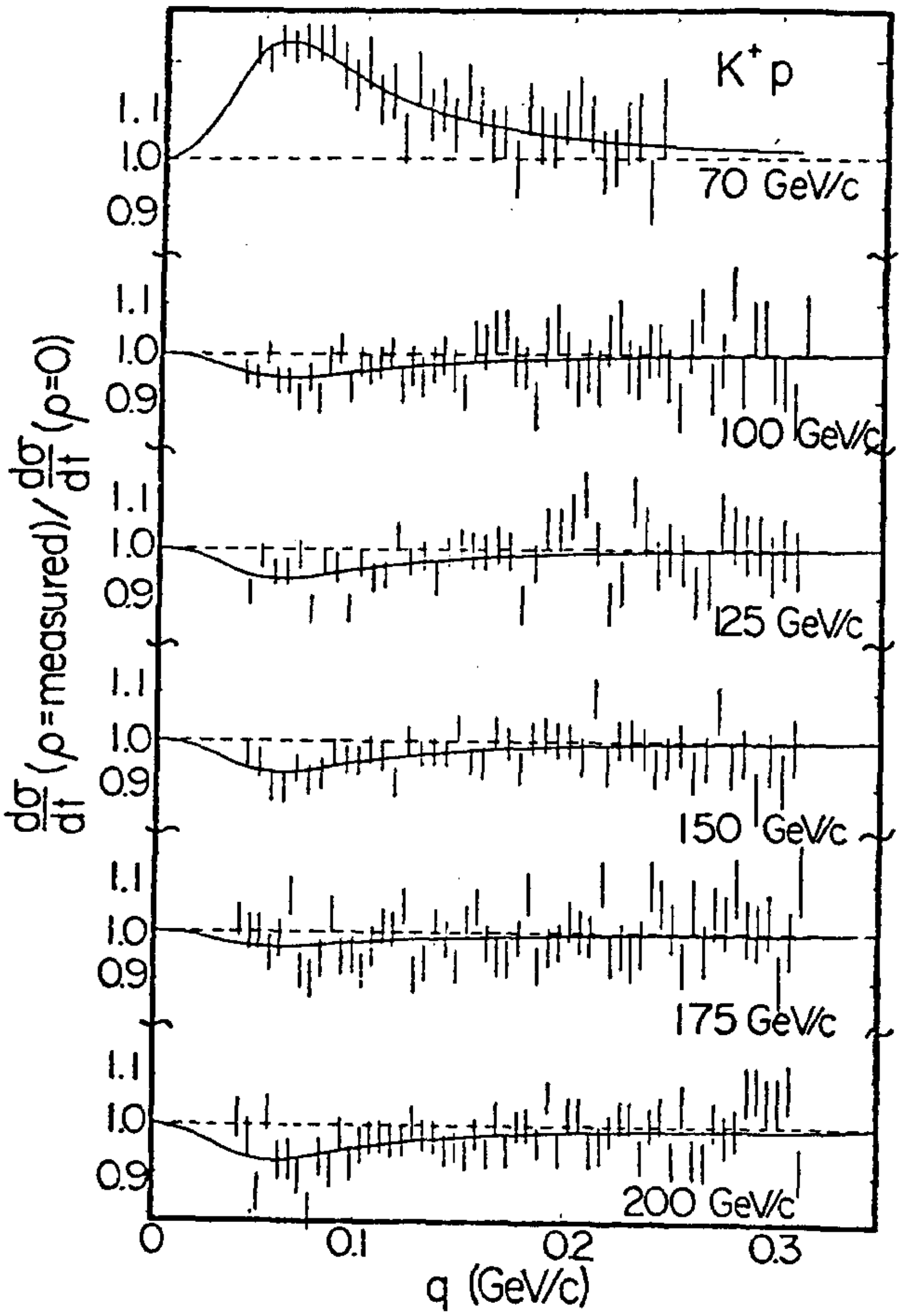
K⁺p
1.1
1.0
0.9
70 GeV/c
100 GeV/c
125 GeV/c
150 GeV/c
175 GeV/c
200 GeV/c
dσ/dt (ρ=measured)/dσ/dt (ρ=0)
0
0.1
0.2
0.3
q (GeV/c)

Figure 12c

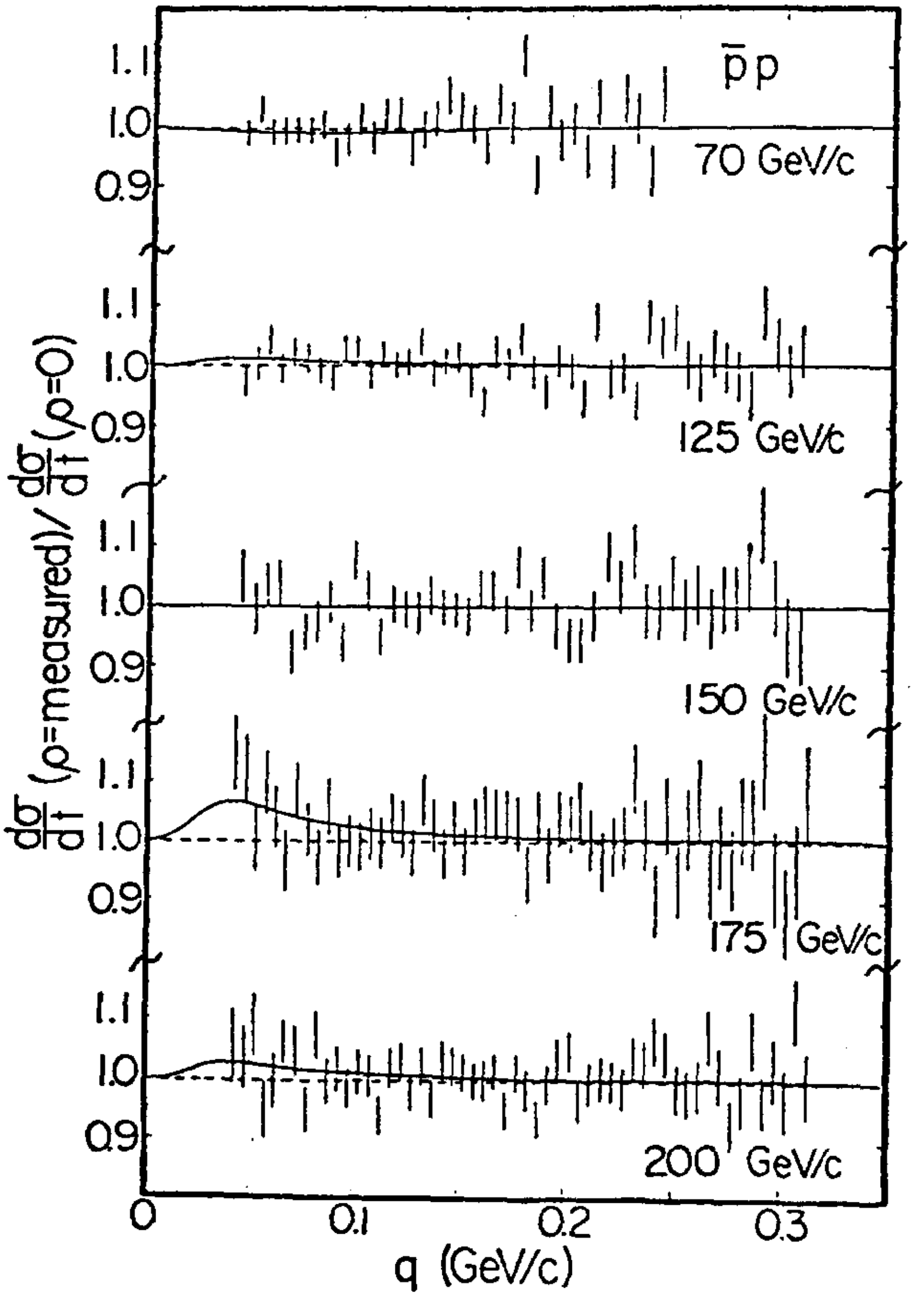
p̄p
70 GeV/c
125 GeV/c
150 GeV/c
175 GeV/c
200 GeV/c
1.1
1.0
0.9
0
0.1
0.2
0.3
q (GeV/c)
dσ/dt (ρ=measured)/ dσ/dt (ρ=0)

Figure 12d

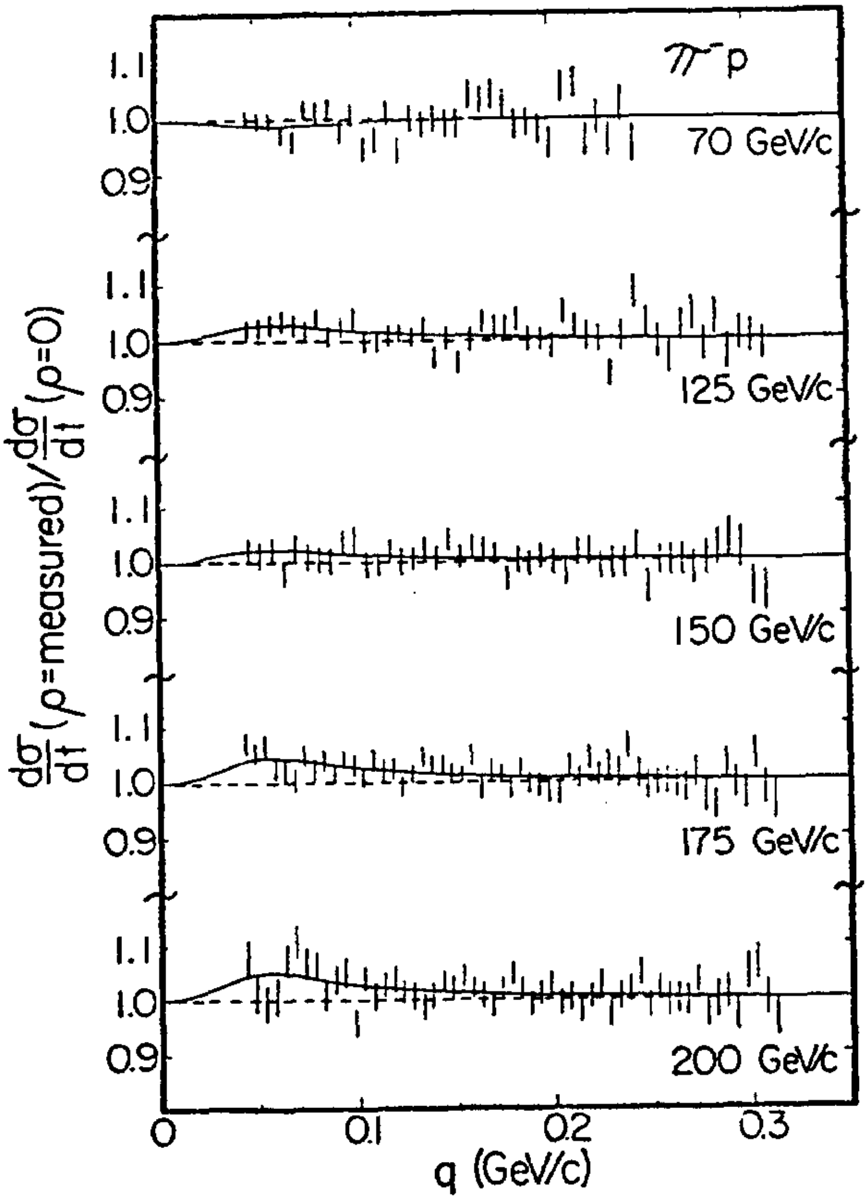

$\pi^- p$
70 GeV/c
125 GeV/c
150 GeV/c
175 GeV/c
200 GeV/c
1.1
1.0
0.9
$\frac{d\sigma}{dt}(\rho=\text{measured})/\frac{d\sigma}{dt}(\rho=0)$
0
0.1
0.2
0.3
q (GeV/c)

Figure 12e

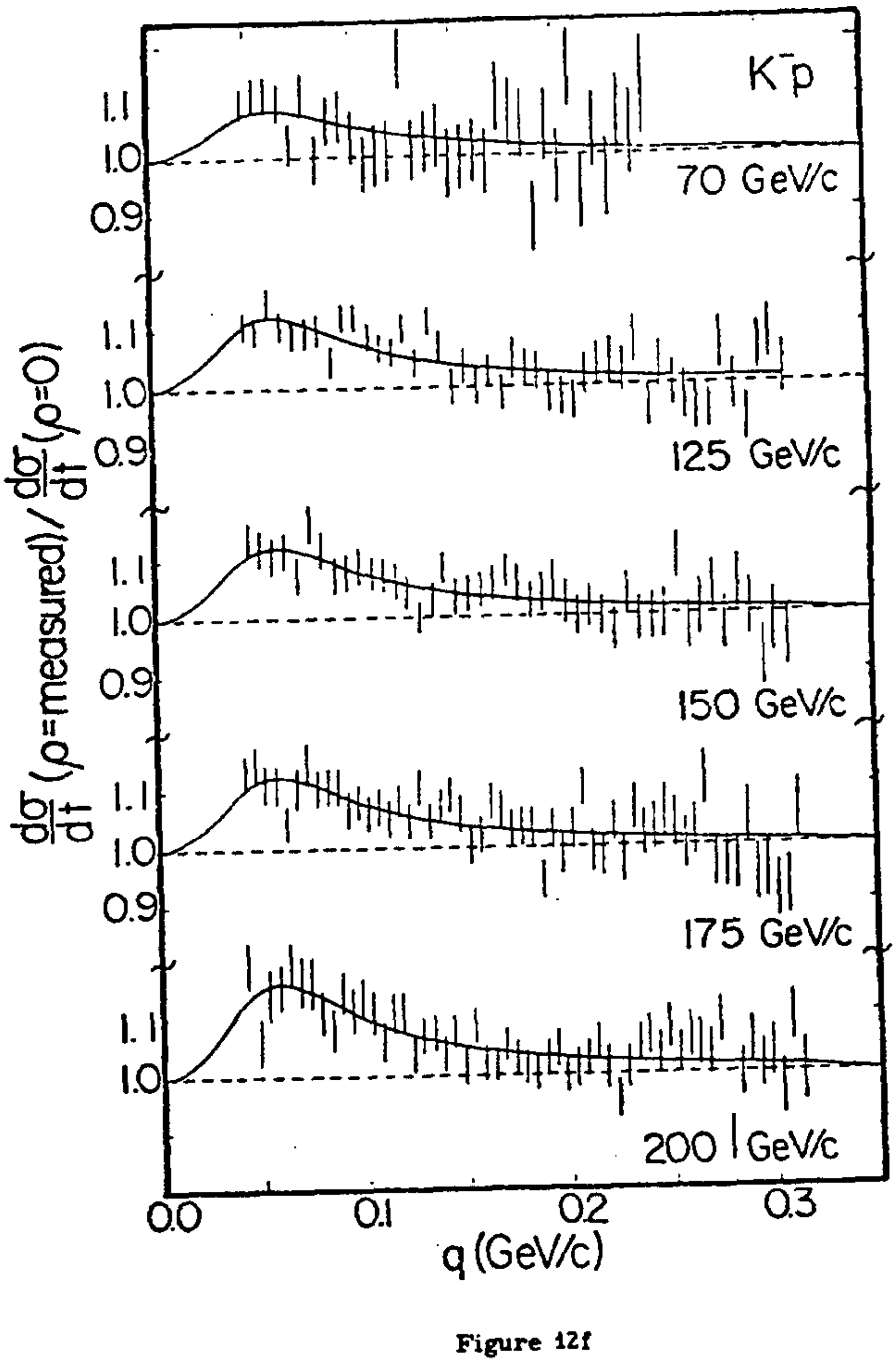
K⁻p
1.1
1.0
0.9
70 GeV/c
125 GeV/c
150 GeV/c
175 GeV/c
200 GeV/c
$\frac{d\sigma}{dt}(\rho=\text{measured})/\frac{d\sigma}{dt}(\rho=0)$
0.0
0.1
0.2
0.3
q (GeV/c)

Figure 12f

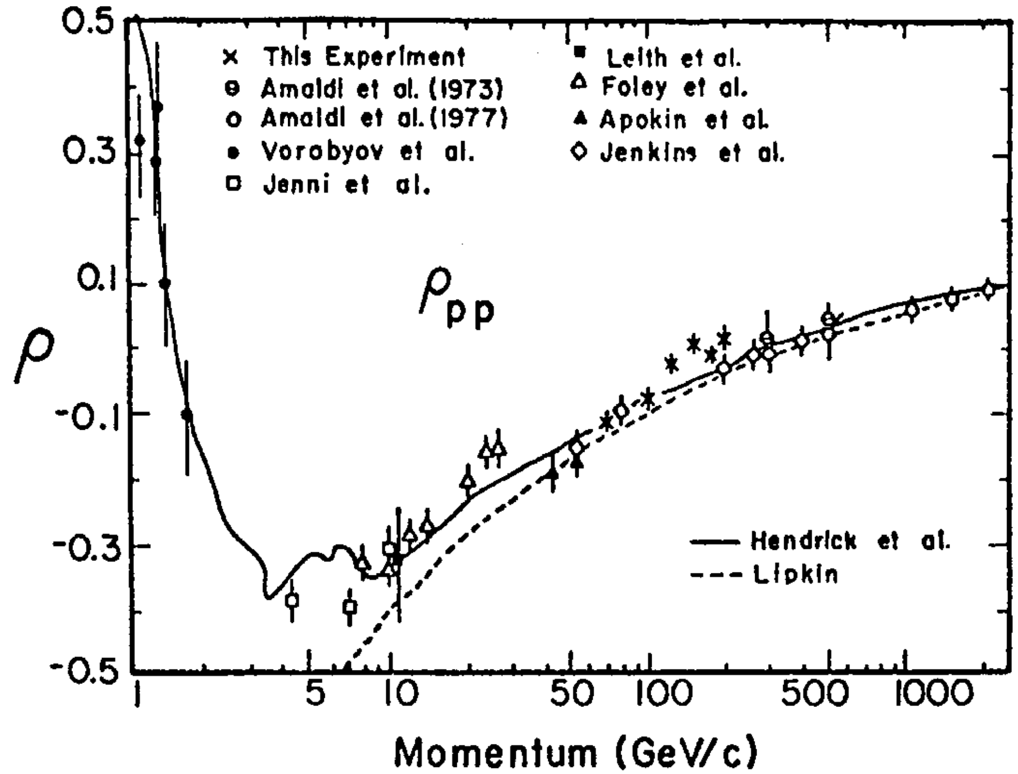
0.5
0.3
0.1
-0.1
-0.3
-0.5
ρ
× This Experiment
⊖ Amaldi et al. (1973)
○ Amaldi et al. (1977)
● Vorobyov et al.
□ Jenni et al.
■ Leith et al.
△ Foley et al.
▲ Apokin et al.
◇ Jenkins et al.
ρ_{pp}
— Hendrick et al.
--- Lipkin
1
5
10
50
100
500
1000
Momentum (GeV/c)

Figure 13a

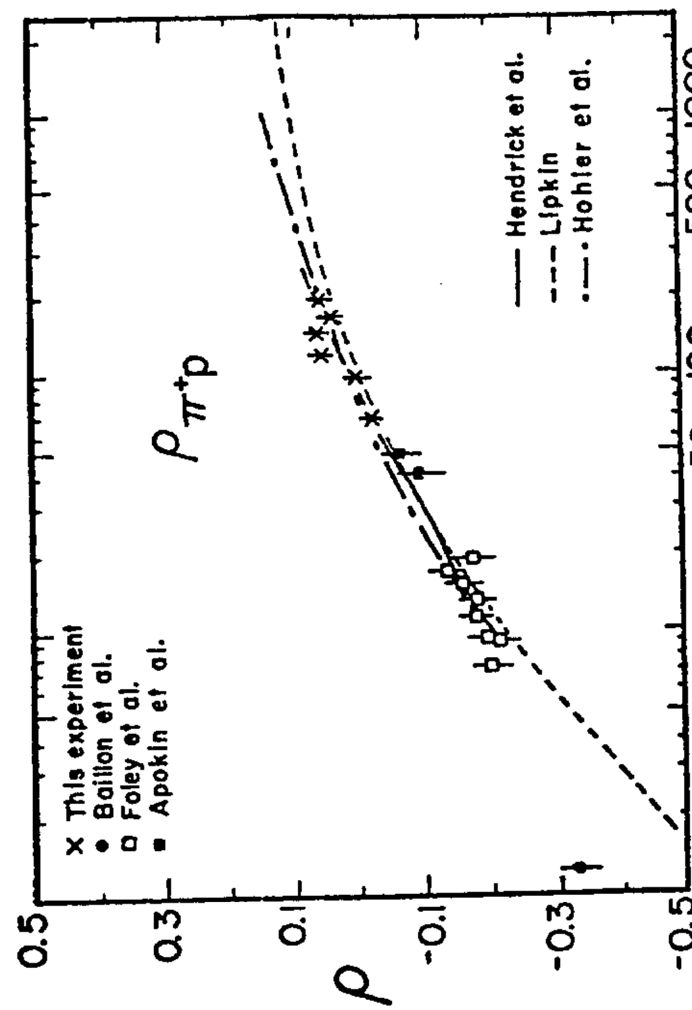
ρ
ρ_{π^+p}
× This experiment
● Baillon et al.
□ Foley et al.
■ Apokin et al.
— Hendrick et al.
- - - Lipkin
-·-·- Hohler et al.
0.5
0.3
0.1
-0.1
-0.3
-0.5
1
5
10
50
100
500
1000
Momentum (GeV/c)

Figure 13b

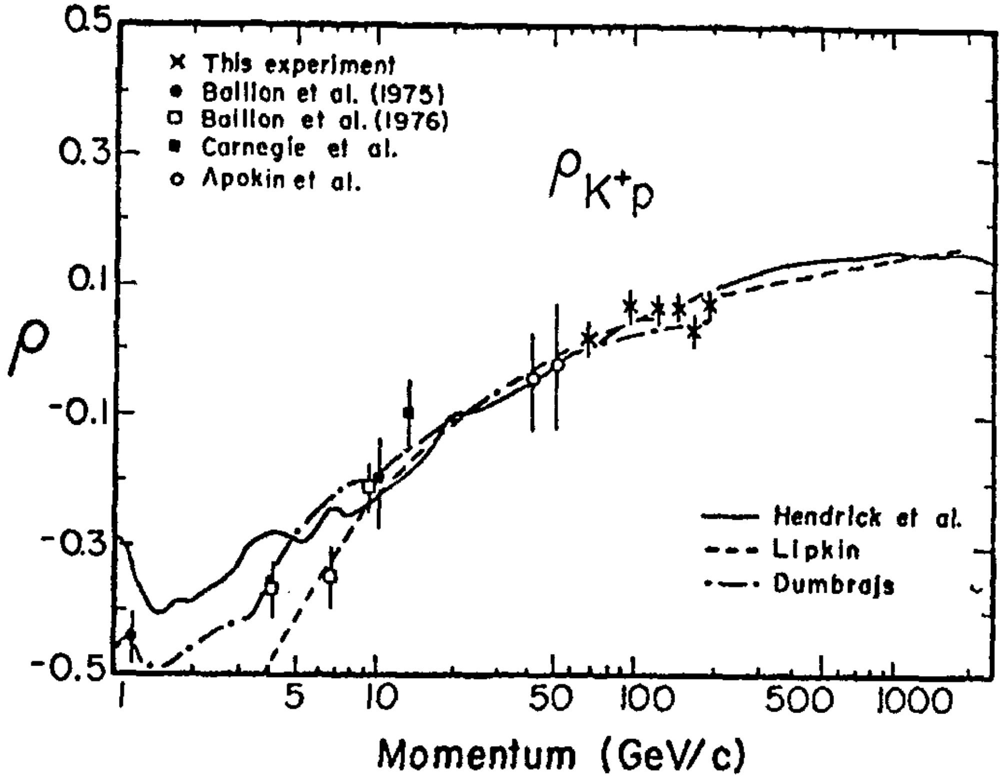

0.5
0.3
0.1
-0.1
-0.3
-0.5
ρ
× This experiment
• Baillon et al. (1975)
□ Baillon et al. (1976)
■ Carnegie et al.
○ Apokin et al.
ρ_{K^+p}
Hendrick et al.
Lipkin
Dumbrajs
1
5
10
50
100
500
1000
Momentum (GeV/c)

Figure 13c

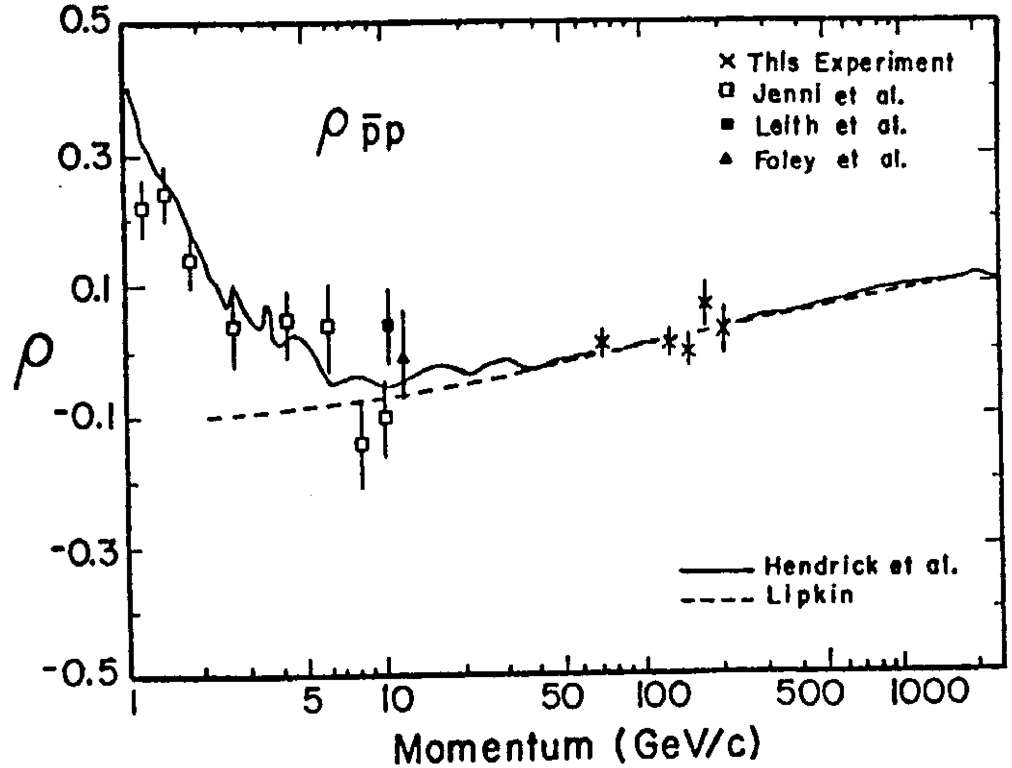

ρ p̄p
× This Experiment
□ Jenni et al.
■ Leith et al.
▲ Foley et al.
—— Hendrick et al.
- - - Lipkin
ρ
0.5
0.3
0.1
-0.1
-0.3
-0.5
1
5
10
50
100
500
1000
Momentum (GeV/c)

Figure 13d

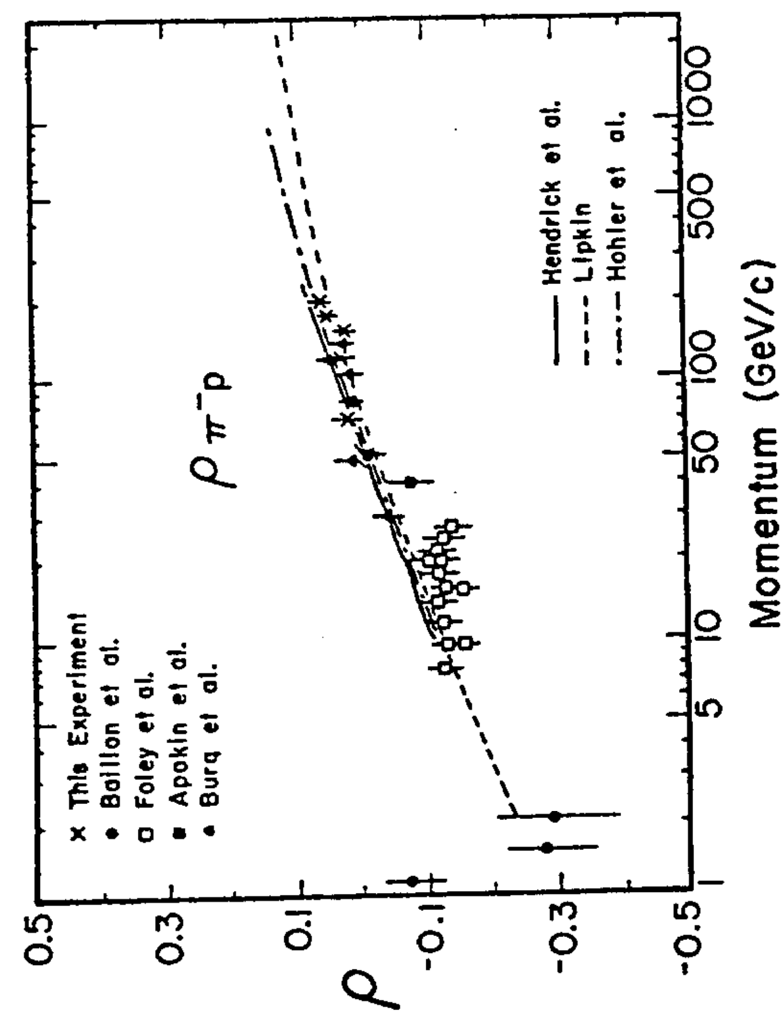
× This Experiment
● Baillon et al.
□ Foley et al.
■ Apokin et al.
▲ Burq et al.
$\rho_{\pi^- p}$
— Hendrick et al.
- - - Lipkin
-·-·- Hohler et al.
ρ
0.5
0.3
0.1
-0.1
-0.3
-0.5
1
5
10
50
100
500
1000
Momentum (GeV/c)

Figure 13e

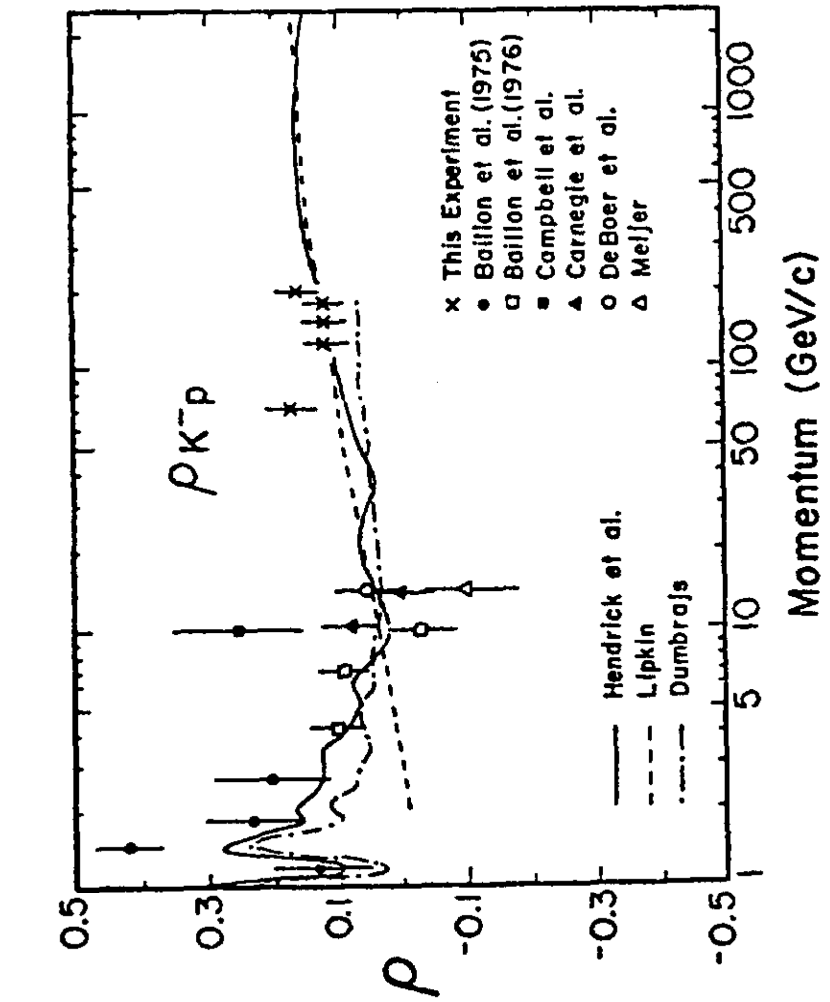

ρ
0.5
0.3
0.1
-0.1
-0.3
-0.5
ρ_{K^-p}
Hendrick et al.
Lipkin
Dumbrajs
× This Experiment
● Baillon et al. (1975)
□ Baillon et al. (1976)
■ Campbell et al.
▲ Carnegie et al.
○ DeBoer et al.
△ Meijer
1
5
10
50
100
500
1000
Momentum (GeV/c)

Figure 13f

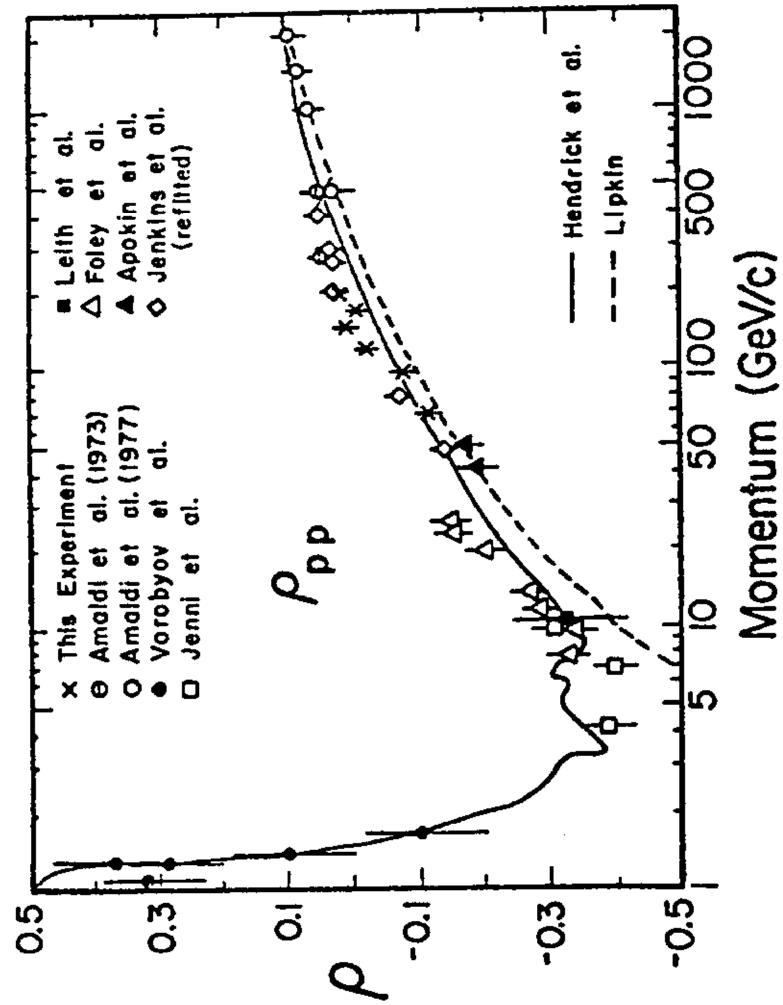
× This Experiment
⊖ Amaldi et al. (1973)
○ Amaldi et al. (1977)
● Vorobyov et al.
□ Jenni et al.
■ Leith et al.
△ Foley et al.
▲ Apokin et al.
◇ Jenkins et al. (refitted)
— Hendrick et al.
- - - Lipkin
ρ_{pp}
ρ
0.5
0.3
0.1
-0.1
-0.3
-0.5
5
10
50
100
500
1000
Momentum (GeV/c)

Figure 14